FBXO24 modulates mRNA alternative splicing and MIWI degradation and is required for normal sperm formation and piRNA production

Zhiming Li[1]*, Xingping Liu[1], Yan Zhang[1], Yuanyuan Li[1], Liquan Zhou[1]*, Shuiqiao Yuan[1,2]*

[1]Institute of Reproductive Health, Tongji Medical College, Huazhong University of Science and Technology, Wuhan 430030, China.

[2]Laboratory of Animal Center, Huazhong University of Science and Technology, Wuhan 430030, China

*Co-correspondence authors.

*Correspondence and requests for materials should be addressed to Dr. Shuiqiao Yuan, Dr. Liquan Zhou, and Dr. Zhiming Li at Institute Reproductive Health, Tongji Medical College, Huazhong University of Science and Technology, Wuhan, Hubei, 430030, China

Emails: shuiqiaoyuan@hust.edu.cn; zhouliquan@hust.edu.cn; lzmleo@hust.edu.cn

Fax: +86 02783692651

Abstract

Spermiogenesis is a critical, post-meiotic phase of male gametogenesis, in which the proper gene expression is essential for sperm maturation. However, the underlying molecular mechanism that controls mRNA expression in the round spermatids remains elusive. Here, we identify that FBXO24, an orphan F-box protein, is highly expressed in the testis of humans and mice and interacts with the splicing factors (SRSF2, SRSF3, and SRSF9) to modulate the gene alternative splicing in the round spermatids. Genetic mutation of FBXO24 in mice causes many abnormal splicing events in round spermatids, thus affecting a large number of critical genes related to sperm formation that were dysregulated. Further molecular and phenotypical analyses revealed that FBXO24 deficiency results in aberrant histone retention, incomplete axonemes, oversized chromatoid body (CB), and abnormal mitochondrial coiling along sperm flagella, ultimately leading to male sterility. In addition, we discovered that FBXO24 interacts with MIWI and SCF subunits and mediates the degradation of MIWI via K48-linked polyubiquitination. Furthermore, we show that FBXO24 depletion could lead to aberrant piRNA production in testes, which suggests FBXO24 is required for normal piRNA biogenesis. Collectively, these data demonstrate that FBXO24 is essential for sperm formation and piRNA production by regulating mRNA alternative splicing and MIWI degradation during spermiogenesis.

Keywords: FBXO24, MIWI, alternative splicing, mitochondria, piRNA, spermiogenesis

Introduction

Spermatogenesis is a dynamic but well-organized process in which germ cells develop in the seminiferous tubules of the testis. Spermatogenesis comprises three phases: mitosis of the spermatogonia, meiosis of spermatocytes, and differentiation of round spermatids into mature sperm. The third phase is also known as spermiogenesis. During spermiogenesis, round spermatids undergo many significant changes, including the loss of cytoplasm, migration of cytoplasmic organelles, formation of the acrosome and flagellum, condensation of nuclei, and reorganization of mitochondria around the sperm midpiece (1). In mice, spermiogenesis is subdivided into 16 steps based on changes in acrosome structure and nuclear compaction (2,3). Coordinated regulation of gene expressions in the round spermatids is essential for sperm formation. However, the underlying molecular mechanism that controls mRNA expression during spermiogenesis remains elusive.

FBXO24 (F-Box Protein 24) is a member of the F-box protein family characterized by an F-box domain. The F-box proteins constitute one of the subunits of the ubiquitin protein ligase complex called SCF (SKP1-cullin-F-box). The interaction between FBXO24 and the SCF subunits is unknown. The F-box domain recruits the F-box protein to the SCF complex, and the carboxy-terminal domain functions as protein-protein interaction. According to the different substrate recognition domains, F-box protein was generally divided into three subclasses: F-box/WD repeat-containing protein (FBXW), leucine-rich repeat protein (FBXL), and F-box only protein (FBXO) with/without other unknown domain (4). Compared with the studies of FBXW and FBXL, the roles of most members of the FBXO subfamily have yet to be defined. FBXO24 belongs to the FBXO class. Previous studies demonstrated some FBXO proteins could regulate spermatogenesis. For example, FBXO47 has been reported to be essential for meiosis I progression in the spermatocytes of mouse testis (5,6), and FBXO43 was associated with male infertility and teratozoospermia (7). In addition, FBXO24 has been reported to recognize deacetylated nucleoside diphosphate kinase A (NDPK-A) to enhance its degradation in HeLa cells (8). In H1299 cells, FBXO24 could promote cell proliferation by mediating ubiquitination and degradation of protein arginine methyltransferase 6 (PRMT6) (9). However, the molecular and biological functions of FBXO24 in mammals remain unclear, especially its role in male fertility and spermatogenesis.

In this study, we find that FBXO24 transcript is abundantly expressed in the testis of humans

and mice. The loss function of FBXO24 in mice resulted in male sterility, with sperm possessing a collapsed mitochondrial sheath and uncompacted chromatin. We revealed that FBXO24 interacts with splicing factors (e.g., SRSF2, SRSF3, and SRSF9) to mediate gene expressions during spermiogenesis. Unexpectedly, we discovered that FBXO24 mediates MIWI ubiquitination and regulates the chromatoid body (CB) architecture and piRNA production. Together, our study demonstrated that FBXO24 plays a critical role in controlling gene expression in haploid spermatids and sperm formation during spermiogenesis.

Results

FBXO24 expressed in haploid spermatids during spermiogenesis.

Multi-alignment and phylogenetic analysis revealed that *Fbxo24* encodes a highly conserved protein expressed in mammals, including humans and mice (**Figure S1A**). FBXO24 has two domains, F-box and regulator of chromatin condensation 1 (RCC1), which were also highly conserved in humans and mice **(Figure S1B)**. Interestingly, qPCR analysis of multiple mouse organs showed that the mRNA of *Fbxo24* was predominantly expressed in mouse testes **(Figure 1A)**. Consistent with this result, transcription expression of analysis of FBXO24 in various human organs from the GE-mini database revealed FBXO24 also a testis-enriched expression in human testes **(Figure S1C)**. Further qPCR analysis of developmental testes and purified testicular cells showed that FBXO24 mRNA was highly expressed in the round spermatids and elongating spermatids **(Figure 1B-C)**. To examine the protein level of FBXO24 in testes, we then characterized the tissue expression pattern of FBXO24 in various organs from adult *Fbxo24*-HA-tagged transgenic mice. Consistent with the mRNA expression showing a testis-enriched expression of FBXO24, FBXO24$^{HA\text{-}Tag}$ protein was exclusively expressed in the testes **(Figure 1D)**, suggesting FBXO24 plays a role during spermatogenesis. To explore the subcellular localization of FBXO24 in male germ cells, we performed immunofluorescence analysis by co-staining of FBXO24$^{HA\text{-}Tag}$ with γ-H2AX (a marker of meiotic DNA damage response) or PNA (an acrosome marker) in adult *Fbxo24*-HA-Tagged transgenic mouse testes. The results showed that FBXO24 $^{HA\text{-}Tag}$ protein was exclusively localized in the nuclei and cytoplasm of spermatids at stages VI-IX **(Figure 1E-F)**, demonstrating FBXO24 expressed in the round and elongating spermatids at steps 6-9. These results

indicate that FBXO24 is an evolutionarily conserved testis-enriched protein expressed in haploid spermatids specifically during spermiogenesis.

FBXO24 deficiency results in detective spermiogenesis and male infertility in mice

To reveal the role of FBXO24 in male germ cell development and spermatogenesis, we generated *Fbxo24* knockout (KO) mice using CRISPR/Cas9 gene editing technology. Two small guide RNAs (sgRNAs) were designed to target exon 3, which encodes the conserved F-box domain **(Figure S2A)**. To validate nucleotide deletion at the targeted loci, the corresponding genomic regions of *Fbxo24* were evaluated by PCR **(Figure S2B)**. qPCR analysis verified the mRNA expression of *Fbxo24* was almost undetectable in *Fbxo24* KO mouse testes **(Figure 2A)**. To test the fecundity of *Fbxo24* KO mice, we crossed *Fbxo24* KO mice with fertility-proved WT mice for at least 6 months. The fertility test results showed that *Fbxo24* KO males were completely infertile, but the *Fbxo24* KO females were fertile **(Figure 2B)**. Interestingly, we observed the testis size and the ratio of testis weight to body weight were comparable between *Fbxo24* KO males and controls **(Figure 2C** and **Figure S2C)**. Consistent with these observations, histological analysis of adult testes and epididymides showed no obvious abnormalities in *Fbxo24* KO mice compared with WT **(Figure S2D)**. However, in *Fbxo24* KO mice, we found fewer elongating spermatids (at stages IX-X) and condensing spermatids (at stages XII) and a reduced number of condensed spermatids (at stages II-VIII) **(Figure 2D-E)**, concomitant with increased apoptotic signals detected in late spermatids **(Figure S2E-F)**, which suggesting FBXO24 deficiency could affect spermatid development during spermiogenesis. To further demonstrate the critical function of FBXO24 during spermiogenesis, we attempted to use the *Fbxo24*-HA-tagged transgenic mice to rescue spermatogenesis and fertility in *Fbxo24* KO males. As expected, we found that expression of the transgenic FBXO24 could rescue the defects in spermiogenesis and infertility observed in *Fbxo24* KO male mice **(Figure 2F and Figure S2G)**, which confirmed the specific targeting of *Fbxo24* in the mutants and the true role of FBXO24 in spermiogenesis. Together, these data indicate that depletion of FBXO24 causes defective spermiogenesis, leading to male infertility.

Ablation of FBXO24 in mice causes disorganized mitochondrial sheath of spermatozoa

To elucidate the causes of sterility in *Fbxo24* KO males, we examined sperm count, sperm motility, and sperm morphology in *Fbxo24* KO mice. The results showed that the sperm count and motility were significantly reduced in *Fbxo24* KO mice compared with WT **(Figure 3A-B)**. Inspiringly, we found that most of the spermatozoa in *Fbxo24* KO mice displayed a disorganized mitochondrial sheath and had abnormal bending of the flagella **(Figure 3C**). In WT spermatozoa, the midpiece connected smoothly to the principal piece; however, in *Fbxo24* KO spermatozoa, a gap in the midpiece can be observed **(Figure 3C-D)**, which may lead to an abrupt bending of the tail. In addition, we observed the midpiece length was significantly shorter in *Fbxo24* KO mouse spermatozoa compared with WT (21.67 ± 1.524 μm in WT *vs*. 14.80 ± 3.430 μm in *Fbxo24* KO) **(Figure 3E)**. To better reveal spermatozoon abnormalities in *Fbxo24* KO mice, we decided to examine the ultrastructure of the spermatozoa using a scanning electron microscope (SEM). In WT spermatozoa, the midpiece was normally populated with many mitochondria in a spiraling fashion. However, in *Fbxo24* KO spermatozoa, mitochondria near the annulus were absent, resulting in a shorter mitochondrial sheath **(Figure 3F)**. Transmission electron microscope (TEM) further confirmed that mitochondria were not present near the annulus or neck and left apparent gaps along the mitochondrial sheath in *Fbxo24* KO spermatozoa **(Figure 3G)**, indicating mitochondrial sheath formation was disrupted. In addition, some mitochondria in the midpiece of *Fbxo24* KO spermatozoa appeared large and swollen. To determine whether the failure in the assembly of the mitochondrial sheath could cause disrupted flagellar development, we examined cross-sections of the *Fbxo24* KO sperm flagellum. In the midpiece, well-defined outer dense fibers (ODFs) and the axoneme consisting of the typical “9 + 2” microtubules were observed in WT spermatozoa, whereas the *Fbxo24* KO spermatozoa displayed incomplete axonemes with missing axonemal microtubules **(Figure 3H)**. In the principal piece, the *Fbxo24* KO spermatozoa also showed completely or partially lacking ODFs and a typical “9 + 2” microtubular structure **(Figure 3H)**. These severe flagellar defects may explain why *Fbxo24* KO spermatozoa displayed decreased motility **(Figure 3B)**.

We next asked whether FBXO24 deletion influences the protein levels of mitochondrial and flagellum components in spermatozoa using Western blot analysis of *Fbxo24* KO spermatozoa. We found that the levels of MFN2 (a marker of mitochondrial fusion) and DRP1 (a marker of mitochondrial fission) were decreased in *Fbxo24* KO spermatozoa **(Figure 3I)**. Moreover, the

protein expression of ODF2, AKAP3, and TSSK4, which were directly related to the formation of the sperm tail (10-12), were all decreased in *Fbxo24* KO spermatozoa **(Figure 3J).** This was supported by the fact that immunofluorescence analysis of ODF2 and AKAP3 on *Fbxo24* KO flagella showed a reduction in their fluorescent signals **(Figure S3A-B)**. Interestingly, we found that the level of the CUL1, a scaffold for E3 ubiquitin ligase, was also significantly reduced in *Fbxo24* KO spermatozoa **(Figure 3J)**. Together, these results indicate that FBXO24 is critical for mitochondrial sheath formation and could modulate the protein expression levels of mitochondrial and flagellar components to maintain sperm motility.

The mitochondrial and chromatoid body architecture were affected in FBXO24-deficient round spermatids

To further explored whether the mitochondrial organelle morphology in round spermatids was affected upon FBXO24 depletion, we examined the ultrastructure of round spermatids from control and *Fbxo24* KO testes by TEM. Notably, we found that the mitochondria displayed swollen and had abnormal central cristae in the round spermatids of *Fbxo24* KO testis **(Figure 4A-B)**. Interestingly, we identified that the chromatoid body (CB) was structurally maintained in *Fbxo24* KO round spermatids, whereas the size was often larger than WT **(Figure 4C-D)**. CB was considered to have the functions in the assembly of the mitochondria during the spermiogenesis, and dysfunctional transformation of the CB in mouse spermatids could cause spermatozoa to possess a collapsed mitochondrial sheath (13), which resembled the phenotype observed in our *Fbxo24* KO mice. To explore the molecular reason for the abnormal CB formation, we examined the protein expression levels of CB components in WT and *Fbxo24* KO testes. Western blot analyses revealed that the protein level of MIWI was remarkably increased in the *Fbxo24* KO testes compared with WT **(Figure 4E)**. However, the level of other proteins of CB and PRMT6 (reported to be the substrate of FBXO24 (9)) appeared to be unchanged in *Fbxo24* KO testes compared with WT **(Figure 4E)**. These results suggest that FBXO24 is essential for maintaining the mitochondria and CB architecture in the normal testis.

Histones failed to be replaced in FBXO24-deficient mouse spermatozoa

To investigate the nuclear morphology of spermatozoa, we examined the sperm head structures of WT and *Fbxo24* KO spermatozoa by SEM. The *Fbxo24* KO spermatozoa exhibited abnormal head morphologies that deviated from the flat, crescent-shaped structures of their WT counterparts **(Figure 4A)**. Specifically, the defects of *Fbxo24* KO spermatozoa included a disorganized anterior acrosome (AS) and the absence of a distinct equatorial segment (EQ), post-acrosomal sheath (PAS), ventral spur (VS), and sharp hook rim (HR) **(Figure 5A)**. TEM analysis further revealed less condensed nuclei of *Fbxo24* KO spermatozoa **(Figure 5B)**, suggesting an abnormal nuclear chromatin compaction was affected in the *Fbxo24* KO sperm head. We then investigated the potential causes of abnormal head structures in *Fbxo24* KO spermatozoa. Given that impaired histone-to-protamine exchange can result in less-condensed nuclei in spermatozoa, we examined histone and protamine levels in *Fbxo24* KO mouse sperm. Western blot revealed increased levels of all core histones H2A, H2B, H3, H4, and transition protein TNP1 but reduced levels of PRM2 in *Fbxo24* KO sperm **(Figure 5C-D)**. Moreover, we found a reduced protein level of PHF7, TSSK6, and RNF8 in *Fbxo24* KO sperm **(Figure 5E-F)**, which have been reported to regulate the chromatin structure to facilitate histone-to-protamine replacement (1,14,15). These data suggest that FBXO24 deletion causes an incomplete histone-to-protamine exchange and defective chromatin compaction during spermiogenesis.

FBXO24 depletion leads to altered gene expressions in the round spermatids

To further investigate the underlying molecular changes during spermatogenesis upon FBXO24 depletion in mice, we performed RNA-seq using purified round spermatids (RS) from adult *Fbxo24* KO and WT males **(Figure S4A)**. A large number of genes significantly differentiated expressed in *Fbxo24* KO round spermatids, including 5368 upregulated and 4097 downregulated genes **(Figure 6A** and **Table S1)**. The Gene Ontology (GO) analysis revealed that the downregulated genes were related to mitochondrion localization, chromatin organization, and protein K48-linked ubiquitination **(Figure 6B** and **Table S2)**. The expression of many genes that are critical for mitochondrion localization (e.g., *Hif1a*, *Nefl*, *Mgarp*, *Zmynd12*, *Map7d1*, *Bbs7*, *Mfn1*, *Ube2j2*) and chromatin organization (e.g., *Rnf20*, *Ep300*, *Sirt1*, *Hmgb2*, *Hsf1*, *Cul4b*, *Kat5*, *Phf7*) was significantly decreased in *Fbxo24* KO round spermatids **(Figure 6C-D)**. Interestingly, we found that *Sept4* and

Sept12, the members of *Septin* family known to generate annuli of spermatozoa, were also downregulated in *Fbxo24* KO round spermatids **(Figure S4B)**. The most upregulated genes in *Fbxo24* KO round spermatids were mainly related to cellular metabolic processes and organelle organization **(Figure S4C)**. Furthermore, we identified an overlap between the downregulated genes and the altered alternative splicing (AS) genes in *Fbxo24* KO round spermatids **(Figure 6E)**. A large number of mRNA splicing changes were identified in *Fbxo24* KO round spermatids **(Figure 6F)**, including skipped exons (SE), alternative 5' splice sites (A5SS), alternative 3' splice sites (A3SS), mutually exclusive exons (MXE), and retained introns (RI). Thus, the RNA-seq data revealed genetic ablation of FBXO24 has a significant impact on the transcriptome of round spermatids, indicating that FBXO24 is required for gene expression in round spermatids during spermiogenesis.

Loss of FBXO24 results in aberrant mRNA alternative splicing in the round spermatids

Since FBXO24 is mainly confined to the nucleus of the round spermatids, we speculated that FBXO24 might interact with the key splicing factors. To test this hypothesis, we performed immunoprecipitation-mass spectrometry (IP-MS) using the HA antibody to unbiasedly identify the interactome of FBXO24 in testes. The IP-MS results showed many splicing factors, such as SRSF2, SRSF3, and SRSF9, highly enriched in HA-immunoprecipitates (**Table S3**). Through co-immunoprecipitation (Co-IP) assays, we confirmed FBXO24 has indeed interacted with splicing factors SRSF2, SRSF3, and SRSF9 in the testes **(Figure 7A)**. Interestingly, we found a significant decrease in SRSF2, SRSF3, and SRSF9 protein expression levels in *Fbxo24* KO testes compared to controls **(Figure 7B-C)**. Because many alternative splicing genes related to sperm formation were affected in *Fbxo24* KO round spermatids by RNA-seq analysis **(Figure 6E)**, we asked if the splicing levels of corresponding exons of those genes were altered. To this end, we performed RT-PCR on purified round spermatids to verify the alternative splicing alteration. The RT-PCR results showed that many genes related to sperm formation, including mitochondria (*Mfn1*), flagellum (*Zmynd12*, *Map7d1*, and *Bbs7*), chromatin (*Phf7* and *Kat5*), acrosome (*Nucb2*), appeared to be significantly alternative splicing changes in their corresponding exons (**Figure 7D-G**). In addition, we found that the alternative splicing of *Ube2j2*, a ubiquitin-conjugating enzyme, was also affected in *Fbxo24* KO round spermatids (**Figure 7H**). Of note, sperm motility was severely impaired in *Ube2j1* KO mice

(16), similar to *Fbxo24* KO mice. Together, these results indicate that FBXO24 could interplay with key splicing factors to regulate the mRNA splicing of some essential genes related to sperm formation.

FBXO24 mediates K48-linked polyubiquitination of MIWI

Since the ectopic expression of MIWI was found in the testes of *Fbxo24* KO mice, we sought to determine whether FBXO24 interacts with MIWI and affects its degradation via ubiquitination. We ectopically expressed FBXO24-mCherry in HEK293T cells, in which MIWI and CUL1 were detected in FBXO24 immunoprecipitates **(Figure 8A)**, suggesting that FBXO24 could bind MIWI and CUL1 *in vivo*. To confirm that FBXO24 endogenously interacted with its candidates in the testes, we performed immunoprecipitation in the testis of *Fbxo24*-HA-tagged transgenic mice. Through co-immunoprecipitation assays, we identified that FBXO24 indeed interacts with MIWI and SCF subunits, CUL1, SKP1and RBX1. **(Figure 8B)**. To further dissect the binding abilities between FBXO24 and MIWI, we examined which domain was responsible for the interaction through the truncated proteins of FBXO24, which only contain the F-box or RCC1 domain **(Figure 8C)**. The immunoprecipitation results showed that both the F-box and RCC1 domains of FBXO24 could bind with MIWI **(Figure 8D)**. Furthermore, we found that FBXO24 leads to a decreased level of MIWI in a concentration-dependent manner, suggesting FBXO24 modulates the degradation of MIWI **(Figure 8E)**. Because K48- and /or K63-linked polyubiquitination was reported to be responsible for degradation, trafficking, and phosphatase activation (17), we then asked which kind of modification participates in MIWI ubiquitination. The immunoblotting results showed that FBXO24 leads to the polyubiquitination of MIWI in the presence of Ub (K48) but not Ub (K63) **(Figure 8F)**. Consistently, FBXO24 contributes to the decreased expression of MIWI in a ubiquitin-dependent manner **(Figure 8G)**. These data suggest that FBXO24 interacts with SCF subunits and mediates the degradation of MIWI via K48-linked polyubiquitination.

FBXO24 is required for normal piRNA production in the testes

Because piRNAs could be loaded onto MIWI (18), we next examined whether the population of piRNAs was affected in *Fbxo24* KO testes. Sequencing of small RNA libraries constructed from

total RNA revealed that the expression of miRNAs was not extensively changed in *Fbxo24* KO testes, with only 20 up- and 13 down-regulated miRNAs **(Figure 9A, Figure S5A,** and **Table S4**). However, a large number of piRNAs were identified to be differentially expressed in *Fbxo24* KO testes, 463 up- and 128 down-regulated piRNAs **(Figure S5B and Table S5)**. After normalized with miRNA counts, the relative amount of total piRNAs was also increased in *Fbxo24* KO testes **(Figure S5C)**. Specifically, an increased piRNAs profile was observed in the genomic regions between 2 kb upstream of transcriptional start sites (TSS) and 2 kb downstream of transcriptional end sites (TES) in *Fbxo24* KO testes **(Figure 9B)**. To assess the potential functions of the association of piRNAs to different functional gene regions, we analyzed the piRNAs mapping density of varying gene regions, including coding region (CDS), 5′ and 3′ untranslated region (UTR), and intron, as well as transposable element (TE), including retrotransposon (LTR, LINE, and SINE) and DNA transposon. The results showed that the intron- and retrotransposon-derived piRNAs were the most affected types in *Fbxo24* KO testes **(Figure 9C and Table S6)**. Furthermore, we analyzed the abundance and size of piRNA populations in adult *Fbxo24* KO and WT testes. The results showed that the number of 29–31nt piRNAs were remarkably increased in *Fbxo24* KO testes compared with WT **(Figure 9D)**. In addition, we found many up-regulated piRNAs in *Fbxo24* KO testes were also presented in previously published data of MIWI immunoprecipitates (19) **(Figure 9E)**, suggesting that the increased piRNAs were MIWI-bound piRNAs. The first nucleotide and 10th nucleotide of repeat piRNAs of *Fbxo24* KO testes exhibited a similar strong bias compared with piRNAs of WT testes, indicating the amplification process of the ping-pong cycle was not affected **(Figure S5D)**. Together, these results show that the loss function of FBXO24 results in aberrant piRNA production in testes, which suggests FBXO24 is required for normal piRNA biogenesis.

Discussion

In this study, we identified FBXO24 as a testis-enriched F-box protein conserved in mammals and highly expressed in the round spermatids and elongating spermatids. To define its biological roles *in vivo*, we generated genetically engineered *Fbxo24* knockout and *Fbxo24* HA-tagged knock-in mouse models. Our functional study demonstrated that FBXO24 is essential for spermiogenesis and piRNA production. FBXO24 deficiency leads to remarkable histone retention

and the disruption of histone-to-protamine transition in the mature sperm. A growing number of studies have demonstrated impaired chromatin condensation can cause nuclear damages as DNA denaturation or fragmentation often associated with male infertility (20). The molecular basis of nuclear condensation is related to key events such as the expression of testis-specific histone variants, post-translational modifications of histones, and transient DNA strand breaks. Indeed, we found that, in the current study, FBXO24 could modulate the homeostasis of PHF7, TSSK6, and RNF8, which are related to the histone-to-protamine transition (1,14,21).

Although the abnormalities of mitochondrial sheaths are observed in infertile men (22), the key proteins implicated in sperm mitochondrial sheath formation largely remain unclear due to a lack of good animal models with the typical phenotype. Notably, we found that the round spermatids and spermatozoon of *Fbxo24* KO mice have impaired mitochondrial architecture, with mitochondrial size heterogeneity and a more open structure of the mitochondria with less crista. Using MitoTracker staining and an electron microscope, we demonstrated the mitochondrial structure is severely disrupted in *Fbxo24* KO spermatozoa. Previous studies showed abnormalities of the annulus (*Sept4* and *Sept12*) (23,24), and chromatid bodies (*Tssk1* and *Tssk2*) (13,25) can disrupt abnormal mitochondrial coiling. Similarly, the current study revealed that *Fbxo24* regulates spatiotemporal mitochondrial dynamics during spermiogenesis. Our study identified FBXO24 might serve as a critical protein in regulating sperm mitochondrial sheath formation, which expands the knowledge of sperm mitochondria formation. In addition, we found that FBXO24 is indispensable for proper flagellum formation, such as axoneme and ODFs. Therefore, the reduction of sperm motility of *Fbxo24* KO male mice observed in this study might attribute to the uncompleted mitochondrial formation of the middle piece and defective flagellum assembling.

It is worth mentioning that the RNA-seq data of the round spermatids showed that FBXO24 ablation leads to dysregulation in the mRNA expression of many genes related to chromatin, mitochondria, and flagellum, indicating the comprehensive mRNA alternative splicing programs in round spermatids were susceptible to ablation of FBXO24. Combined with our immunoprecipitation assays provided evidence of molecular interactions between FBXO24 and the key splice factors (SRSF2, SRSF3, and SRSF9), it is reasonable to infer that dysregulation of these splicing factors inevitably would lead to more splicing errors in their target genes, thus amplifying the initial adverse

effects and generating a vicious circle of aberrant splicing. Of note, many genetic changes identified in this study have been closely associated with spermatogenesis. For example, *Zmynd12* (26), *Bbs7* (27), and *Ube2j2* (16) were required for flagellum function and male fertility. *Map7d1* facilitates microtubule stabilization (28) and *Mfn1* deficiency leads to defects in mitochondrial activity and male infertility (29). *Phf7* modulates BRDT stability and histone-to-protamine exchange during spermiogenesis (30). *Kat5* encodes an essential lysine acetyltransferase, which is involved in regulating gene expression and chromatin remodeling (31). *Nucb2* suppresses the acrosome reaction in sperm within the mouse epididymis (32). Therefore, our study, for the first time, provides evidence that FBXO24 interacts with the splicing factors in round spermatids to regulate the alternative splicing of mRNA involved in round spermatid development during spermiogenesis. However, the exact regulatory mechanism of how FBXO24 facilitates the mRNA alternative splicing needs further study.

In addition to modulating alternative splicing, we demonstrated that FBXO24 is a novel E3 ligase that can mediate the K48-linked ubiquitination of MIWI. FBXO24 deletion results in the increase of MIWI and piRNA production in the testes. A previous study showed the ubiquitination of MIWI through the APC/C-26S proteasome pathway *in vitro* (33). In the current study, we identified that testis-enriched FBXO24 could interact with MIWI and mediate MIWI degradation, which provides new insight into MIWI degradation during spermiogenesis. MIWI and piRNAs are highly abundant in round spermatids, but their levels start to decline normally in elongating spermatids and are completely eliminated in matured sperm (34). Overexpression of a piRNA cluster in the mouse genome can reduce the expression of mRNA required for spermatogenesis, leading to male infertility. Interestingly, our small RNA-seq results showed FBXO24 deficiency does not have a significant impact on piRNA mapping. However, the level of 29–31nt piRNA was remarkably increased in *Fbxo24* KO testes. Previous studies revealed that MIWI-bound piRNA could cause mRNA decay in the testes (35,36), which raises a possibility that piRNA-related transcriptional repression in *Fbxo24* KO testes might contribute to the reduction of mature sperm in *Fbxo24* KO mice.

In summary, we discovered that FBXO24 is essential for mitochondrial organization and chromatin condensation in the spermatozoa. Our results disclose FBXO24 interacts with splicing factors to regulate the mRNA splicing of some essential genes required to spermiogenesis (**Figure**

10). We demonstrated FBXO24 interplays with the subunits of SCF complex and mediates MIWI degradation via K48-linked polyubiquitination. This study extensively expands our understanding of the regulation of gene expression in the round spermatids.

In summary, our study revealed a novel role for FBXO24 in controlling mRNA alternative splicing of round spermatids and MIWI/piRNA pathway and demonstrated that FBXO24 is required for mitochondrial organization and chromatin condensation in mouse spermatozoa. Importantly, our results disclosed FBXO24 interacts with splicing factors to regulate the mRNA splicing of some essential genes required for spermiogenesis, which probably functionally connects the dysregulation of genes involved in mitochondria migration and histone removal during spermiogenesis (Figure 10). We further demonstrated FBXO24 interplays with the subunits of the SCF complex and mediated MIWI degradation via K48-linked polyubiquitination. This study extensively expands our understanding of the mechanistic explanation of FBXO24 for the regulation of spermiogenesis.

Materials and Methods

Ethics statement

All the animal procedures were approved by the Institutional Animal Care and Use Committee of Tongji Medical College, Huazhong University of Science and Technology, and the mice were housed in the specific pathogen-free facility of Huazhong University of Science and Technology. All experiments with mice were conducted ethically according to the Guide for the Care and Use of Laboratory Animal guidelines.

Generation of *Fbxo24* mutant mice

Fbxo24 knockout (KO) mice were generated by CRISPR/Cas9 technology. Briefly, the two pairs of single-guided RNAs (sgRNAs) with the sequence sgRNA-1: 5’-TGTGGAGGCGCATCTGTCGAAGG-3’ and sgRNA-2 5’-GTCAAAGACTTGGTCGCCCTAGG-3’ were designed for targeting for the third exon of *Fbxo24* gene. The sgRNAs were injected into the pronuclei of fertilized eggs, and the 2-cell stage embryos were transferred into the oviducts of pseudopregnant C57BL/6J females in the next day to generate *Fbxo24* mutant founder mice (F0). The F1 *Fbxo24* heterozygous mice were produced by

crossing the F0 founder mice with WT mice and further intercrossed F1 to obtain *Fbxo24* KO mice carrying an 82-bp deletion in exon 3 of the *Fbxo24* gene. A 197-bp band as the wild-type (WT) allele and a 115-bp band as the deleted allele were designed for genotyping by PCR amplification. The primers used are listed in **Table S7**.

Generation of *Fbxo24*-HA Tagged knock-in (KI) mice

Fbxo24-HA-tagged KI mice were also generated by CRISPR/Cas9 technology and haploid embryonic stem cell microinjection. The sgRNAs of the C-terminus of the target gene *Fbxo24* (AAGAAGAGGGGTTCAGCTCT) were synthesized, annealed, and ligated to the pX330-mCherry plasmid. For the construction of the HA-tag KI DNA donor, the sequences encoding the left homologous arm, the HA tag, and the right homologous arm were amplified and ligated to the linear pMD19T. DKO-AG-haESCs were transfected with CRISPR-Cas9 plasmid and HA tag KI DNA donor. At 24 h after transfection, the mCherry-positive haploid cells were enriched. In 7–8 days after plating, single colonies were picked up, and positive colonies for the HA tag were selected by genomic DNA PCR amplification for Sanger sequencing. DKO-AG-haESCs with *Fbxo24*-C-HA were arrested in M-phase by culturing in a medium containing 0.05 μg/ml demecolcine for 10 h and then used for intracytoplasmic injection as described previously (37). Intracytoplasmic AG-haESC injection (ICAHCI) embryos were cultured in KSOM medium for 24 h to reach the two-cell stage. 15–20 two-cell embryos were transferred into each oviduct of pseudo-pregnant females to produce *Fbxo24*-C-HA semi-cloned mice (F0). Then, the F0 female mice were crossed with WT male mice to generate heterozygous *Fbxo24*-C-HA F1 male mice for the experiments.

Antibodies

The details of all commercial antibodies used in this study are presented in **Table S8.**

Electron microscopy

For transmission electron microscopy (TEM), samples were fixed in 4% paraformaldehyde containing 0.05% glutaraldehyde in 0.1 M PBS, then post-fixed in 1% osmium tetroxide. Dehydration was carried out in ethanol, and the samples were embedded in Epon 812. Ultrathin

sections were counterstained with uranyl acetate and lead citrate and examined with a transmission electron microscope (Hitachi HT7700, Japan). For scanning electron microscopy (SEM), the samples were fixed in 2.5% glutaraldehyde solution in 0.1 M PBS and collected on poly-L-lysine-coated glass coverslips, followed by post-fixed in osmium tetroxide and dehydrated in graded ethanol series. Then, the samples were subjected to critical point drying and coated with gold/palladium for observation with a scanning electron microscope (AZteclive Ultim Max 100, UK).

Histological analysis

Testes and epididymides from WT and KO mice were fixed in Bouin's fixative and embedded in paraffin. For the histological analysis, sections of 5 μm were cut and stained with periodic acid-Schiff (PAS) or hematoxylin and eosin (H&E) after dewaxing and rehydration.

Immunofluorescence

Testes were fixed in 4% PFA in PBS overnight at 4 °C and then were sequentially soaked in 5, 10, 12.5, 15, and 20% sucrose in PBS and embedded in Tissue-Tek O.C.T. compound (Sakura Finetek, 4583) on dry ice. 5 μm cryosections were cut and washed with PBS three times (10 min per wash), then the cryo-sections were microwaved in 0.01 M sodium citrate buffer (pH 6.0) and cooled down to room temperature (RT) for antigen retrieval. After washing with PBS three times, the sections were blocked in a blocking solution (containing 3% normal donkey serum and 3% fetal bovine serum in 1% bovine serum albumin) for 1 h. Then, the sections were incubated with primary antibodies overnight at 4 °C and then incubated with secondary antibodies for 1 h at RT. After washing with PBS and stained with DAPI, the sections were photographed under FluoView 1000 microscope (Olympus, Japan) with a digital camera (MSX2, Micro-shot Technology Limited, China).

TUNEL staining

Testes were fixed in 4% PFA, embedded in Tissue-Tek O.C.T. compound, and cut section with 5 μm-thick. TUNEL staining was performed using the TUNEL ApoGreen Detection Kit (YEASEN, 40307ES20). Images were obtained with a FluoView 1000 microscope (Olympus, Japan).

Western blot

Fresh mouse adult testes or HEK293T cells were collected, and proteins were extracted by using RIPA buffer (Beyotime, P0013J). In total, 40 μg of protein lysates were separated on a 10% SDS-PAGE gel, proteins were transferred to PVDF membranes (Bio-Rad) and the membranes were blocked in 5% non-fat milk (blocking solution) for 1 h. Primary antibodies were incubated overnight at 4 °C after blocking. The membranes were washed with TBST three times and then incubated with a secondary antibody for 1 h before using Luminol/enhancer solution and Peroxide solution (ClarityTM Western ECL Substrate, Bio-Rad).

Immunoprecipitation (IP) assays

For testis tissue IP experiments, the testes were dissected and lysed in immunoprecipitation buffer (Beyotime, P0013J), clarified by centrifugation at 12,000 × g, and then pre-cleared with anti-HA nanobody agarose beads (AlpaLife, ktsm1305). The lysate was incubated with primary antibodies overnight at 4 °C on a rotator and conjugated with anti-HA beads. The beads were washed with IP buffer and then boiled in 2× SDS loading buffer for western blotting analysis.

For cell line IP experiments, the HEK293T cells were transfected with indicated plasmids using Lipofectamine 2000 (Life Technologies). After 48 h, immunoprecipitation was performed as described previously (38). 25 μl mCherry-Trap bead 50% slurry (AlpaLife, ktsm1331) was used and all wash steps were performed with washing buffer (10mM Tris-HCl pH7.5, 150mM NaCl, 0.5mM EDTA). mCherry-Trap beads were washed with dilution buffer prior to addition to the cell lysate. Beads were incubated with cell lysate at 4°C for 2 h following another wash step. To elute the proteins from the beads, 40 μl sample buffer (120 mM Tris-HCl pH=6.8, 20% glycerol, 4% SDS, 0.04% Bromophenol blue, 10% β-mercaptoehanol) was added and boiled at 95°C for 5 min. mCherry-tagged proteins were detected by western blotting using an anti-mCherry antibody.

Spermatogenic cell isolation

Spermatogenic cells were isolated from the whole mouse testis using the STA-PUT method described previously with slight modifications(39). In brief, testes were collected from 8-week-old

mice WT and *Fbxo24* KO mice and decapsulated with collagenase treatment to remove Leydig cells. The dispersed seminiferous tubules were then digested with trypsin and DNase I to single-cell suspensions. Next, Sertoli cells were separated from germ cells by filtration through a 40 mm cell strainer and by adhesion to lectin-coated culture plates. Different germ cell populations were separated using a manually prepared 0.5–5% discontinuous BSA density gradient for velocity sedimentation sediment. After sedimentation, enriched fractions of the round spermatids were manually collected.

RNA isolation and quantitative qPCR

Total RNAs were extracted from purified germ cell fractions using TRIzol reagent (Invitrogen) following the manufacturer's procedure. The purity and concentration of RNA samples were determined using a Nanodrop ND-2000 spectrophotometer (Thermo Scientific). Reverse transcriptional reactions contained 500 ng of purified total RNA using a PrimeScript RT reagent kit with gDNA Eraser (Takara) to remove the DNA contamination. RT-qPCR was performed with SYBR green master mix (Takara) on the ABI Step One System (Applied Biosystems) according to manufactures' instructions. The relative gene expression was quantified using the comparative cycle threshold method, with the *Gapdh* expression used for normalization.

RNA-seq analysis

1 μg of total RNA was used from each group to prepare the mRNA libraries using TruSeq Stranded mRNA Library Preparation Kit Set A (Cat. No. RS-122-2101, Illumina) according to the manufacturer's instructions. All libraries were sequenced using the Illumina HiSeq 4000 platform. The FASTX-Toolkit was used to remove adaptor sequences, and low-quality reads from the sequencing data. To identify all the transcripts, we used Tophat2 and Cufflinks to assemble the sequencing reads based on the UCSC mm10 mouse genome. The differentially expression analysis was performed by Cuffdiff. The differential expressed genes were set with the threshold of $P < 0.05$ and fold-change > 2.

Small RNA-seq and annotation

For small RNA-seq, the total RNA from adult testes was gel fractionated, and those 16–40 nt in length were purified for small RNA-seq. The small RNA libraries were constructed using the Digital Gene Expression for Small RNA Sample prep kit (Illumina). Sequencing of the small RNA library was performed by Illumina HiSeq Xten. Small RNA annotation was performed as described previously (40).

Statistical analysis

All data are presented as mean ± S.D. unless otherwise noted in the figure legends. Statistical differences between datasets were assessed by one-way ANOVA or Student's *t*-test using the GraphPad software. *P*-values are denoted in figures by $*P < 0.05$; $**P < 0.01$; $***P < 0.001$.

Data availability

All data needed to evaluate the conclusions in the paper are present in the article and/or the Supplementary Materials. RNA-seq and Small RNA-seq data are deposited in the NCBI SRA database with the accession number PRJNA878933 and PRJNA878953, respectively.

Funding

This work was supported by National Natural Science Foundation of China (82001620 to Z.L. and 82171605 to S.Y.), the National Key R&D Program of China (2018YFC1004500 to L.Z.) and the Open Research Fund of the National Center for Protein Sciences at Peking University in Beijing (KF-202205 to Z.L.).

Author contributions

Z.L., L.Z., and S.Y. conceived and designed the research. Z.L., X.L., Y.Z., and Y.L. performed the bench experiments and data analysis. L.Z. generated the *Fbxo24* KO mouse model. Z.L. wrote the manuscript. S.Y., L.Z., and Z.L. supervised the project. S.Y., and Z.L. revised the manuscript. All authors read and approved the manuscript.

Conflict of interest

The authors declare no conflict of interest.

References

1. Jha, K.N., Tripurani, S.K. and Johnson, G.R. (2017) TSSK6 is required for gammaH2AX formation and the histone-to-protamine transition during spermiogenesis. *J Cell Sci*, **130**, 1835-1844.
2. Ahmed, E.A. and de Rooij, D.G. (2009) Staging of mouse seminiferous tubule cross-sections. *Methods Mol Biol*, **558**, 263-277.
3. Meistrich, M.L. and Hess, R.A. (2013) Assessment of spermatogenesis through staging of seminiferous tubules. *Methods Mol Biol*, **927**, 299-307.
4. Kipreos, E.T. and Pagano, M. (2000) The F-box protein family. *Genome Biol*, **1**, REVIEWS3002.
5. Hua, R., Wei, H., Liu, C., Zhang, Y., Liu, S., Guo, Y., Cui, Y., Zhang, X., Guo, X., Li, W. *et al.* (2019) FBXO47 regulates telomere-inner nuclear envelope integration by stabilizing TRF2 during meiosis. *Nucleic Acids Res*, **47**, 11755-11770.
6. Tanno, N., Takemoto, K., Takada-Horisawa, Y., Shimada, R., Fujimura, S., Tani, N., Takeda, N., Araki, K. and Ishiguro, K.I. (2022) FBXO47 is essential for preventing the synaptonemal complex from premature disassembly in mouse male meiosis. *iScience*, **25**, 104008.
7. Ma, Y., Xie, N., Xie, D., Sun, L., Li, S., Li, P., Li, Y., Li, J., Dong, Z. and Xie, X. (2019) A novel homozygous FBXO43 mutation associated with male infertility and teratozoospermia in a consanguineous Chinese family. *Fertil Steril*, **111**, 909-917 e901.
8. Chen, W., Xiong, S., Li, J., Li, X., Liu, Y., Zou, C. and Mallampalli, R.K. (2015) The ubiquitin E3 ligase SCF-FBXO24 recognizes deacetylated nucleoside diphosphate kinase A to enhance its degradation. *Mol Cell Biol*, **35**, 1001-1013.
9. Chen, W., Gao, D., Xie, L., Wang, A., Zhao, H., Guo, C., Sun, Y., Nie, Y., Hong, A. and Xiong, S. (2020) SCF-FBXO24 regulates cell proliferation by mediating ubiquitination and degradation of PRMT6. *Biochem Biophys Res Commun*, **530**, 75-81.
10. Wang, X., Wei, Y., Fu, G., Li, H., Saiyin, H., Lin, G., Wang, Z., Chen, S. and Yu, L. (2015) Tssk4 is essential for maintaining the structural integrity of sperm flagellum. *Mol Hum Reprod*, **21**, 136-145.
11. Donkor, F.F., Monnich, M., Czirr, E., Hollemann, T. and Hoyer-Fender, S. (2004) Outer dense fibre protein 2 (ODF2) is a self-interacting centrosomal protein with affinity for microtubules. *J Cell Sci*, **117**, 4643-4651.
12. Xu, K., Yang, L., Zhang, L. and Qi, H. (2020) Lack of AKAP3 disrupts integrity of the subcellular structure and proteome of mouse sperm and causes male sterility. *Development*, **147**.
13. Shang, P., Baarends, W.M., Hoogerbrugge, J., Ooms, M.P., van Cappellen, W.A., de Jong, A.A., Dohle, G.R., van Eenennaam, H., Gossen, J.A. and Grootegoed, J.A. (2010) Functional transformation of the chromatoid body in mouse spermatids requires testis-specific serine/threonine kinases. *J Cell Sci*, **123**, 331-339.
14. Lu, L.Y., Wu, J., Ye, L., Gavrilina, G.B., Saunders, T.L. and Yu, X. (2010) RNF8-dependent histone modifications regulate nucleosome removal during spermatogenesis. *Dev Cell*, **18**, 371-384.
15. Wang, X., Kang, J.Y., Wei, L., Yang, X., Sun, H., Yang, S., Lu, L., Yan, M., Bai, M., Chen, Y. *et al.* (2019) PHF7 is a novel histone H2A E3 ligase prior to histone-to-protamine exchange during spermiogenesis. *Development*, **146**.
16. Koenig, P.A., Nicholls, P.K., Schmidt, F.I., Hagiwara, M., Maruyama, T., Frydman, G.H., Watson, N., Page, D.C. and Ploegh, H.L. (2014) The E2 ubiquitin-conjugating enzyme UBE2J1 is required for spermiogenesis in mice. *J Biol Chem*, **289**, 34490-34502.
17. Tracz, M. and Bialek, W. (2021) Beyond K48 and K63: non-canonical protein ubiquitination. *Cell Mol Biol Lett*, **26**, 1.
18. Kawase, M., Ichiyanagi, K.J.F.i.C. and Biology, D. (2022) The Expression Dynamics of piRNAs Derived From

Male Germline piRNA Clusters and Retrotransposons. 1064.

19. Reuter, M., Berninger, P., Chuma, S., Shah, H., Hosokawa, M., Funaya, C., Antony, C., Sachidanandam, R. and Pillai, R.S. (2011) Miwi catalysis is required for piRNA amplification-independent LINE1 transposon silencing. *Nature*, **480**, 264-267.

20. Filatov, M.V., Semenova, E.V., Vorob'eva, O.A., Leont'eva, O.A. and Drobchenko, E.A. (1999) Relationship between abnormal sperm chromatin packing and IVF results. *Mol Hum Reprod*, **5**, 825-830.

21. Wang, X.K., Kang, J.Y., Wei, L.X., Yang, X.G., Sun, H.D., Yang, S.M., Lu, L., Yan, M., Bai, M.Z., Chen, Y.Y. *et al.* (2019) PHF7 is a novel histone H2A E3 ligase prior to histone-to-protamine exchange during spermiogenesis. *Development*, **146**.

22. Kubo-Irie, M., Matsumiya, K., Iwamoto, T., Kaneko, S. and Ishijima, S. (2005) Morphological abnormalities in the spermatozoa of fertile and infertile men. *Mol Reprod Dev*, **70**, 70-81.

23. Kissel, H., Georgescu, M.M., Larisch, S., Manova, K., Hunnicutt, G.R. and Steller, H. (2005) The Sept4 septin locus is required for sperm terminal differentiation in mice. *Developmental Cell*, **8**, 353-364.

24. Shen, Y.R., Wang, H.Y., Kuo, Y.C., Shih, S.C., Hsu, C.H., Chen, Y.R., Wu, S.R., Wang, C.Y. and Kuo, P.L. (2017) SEPT12 phosphorylation results in loss of the septin ring/sperm annulus, defective sperm motility and poor male fertility. *Plos Genet*, **13**.

25. Dirami, T., Rode, B., Wolf, J.P., Gacon, G., Duliouist, E. and Toure, A. (2015) Assessment of the frequency of sperm annulus defects in a large cohort of patients presenting asthenozoospermia. *Basic Clin Androl*, **25**, 10.

26. Dacheux, D., Martinez, G., Broster Reix, C.E., Beurois, J., Lorès, P., Tounkara, M., Dupuy, J.-W., Robinson, D.R., Loeuillet, C. and Lambert, E.J.b. (2023) Novel axonemal protein ZMYND12 interacts with TTC29 and DNAH1, and is required for male fertility and flagellum function. 2023.2003. 2007.531490.

27. Zhang, Q., Nishimura, D., Vogel, T., Shao, J., Swiderski, R., Yin, T., Searby, C., Carter, C.S., Kim, G., Bugge, K. *et al.* (2013) BBS7 is required for BBSome formation and its absence in mice results in Bardet-Biedl syndrome phenotypes and selective abnormalities in membrane protein trafficking. *J Cell Sci*, **126**, 2372-2380.

28. Kikuchi, K., Sakamoto, Y., Uezu, A., Yamamoto, H., Ishiguro, K.I., Shimamura, K., Saito, T., Hisanaga, S.I. and Nakanishi, H. (2022) Map7D2 and Map7D1 facilitate microtubule stabilization through distinct mechanisms in neuronal cells. *Life Sci Alliance*, **5**.

29. Zhang, J., Wang, Q., Wang, M., Jiang, M., Wang, Y., Sun, Y., Wang, J., Xie, T., Tang, C., Tang, N. *et al.* (2016) GASZ and mitofusin-mediated mitochondrial functions are crucial for spermatogenesis. *EMBO Rep*, **17**, 220-234.

30. Kim, C.R., Noda, T., Kim, H., Kim, G., Park, S., Na, Y., Oura, S., Shimada, K., Bang, I., Ahn, J.Y. *et al.* (2020) PHF7 Modulates BRDT Stability and Histone-to-Protamine Exchange during Spermiogenesis. *Cell Rep*, **32**, 107950.

31. Gehlen-Breitbach, S., Schmid, T., Frob, F., Rodrian, G., Weider, M., Wegner, M. and Golz, L. (2023) The Tip60/Ep400 chromatin remodeling complex impacts basic cellular functions in cranial neural crest-derived tissue during early orofacial development. *Int J Oral Sci*, **15**, 16.

32. Kim, S., Sun, S., Kim, M., Ha, J., Seok, E. and Yang, H. (2023) NUCB2/nesfatin-1 suppresses the acrosome reaction in sperm within the mouse epididymis. *Anim Cells Syst (Seoul)*, **27**, 120-128.

33. Zhao, S., Gou, L.T., Zhang, M., Zu, L.D., Hua, M.M., Hua, Y., Shi, H.J., Li, Y., Li, J., Li, D. *et al.* (2013) piRNA-triggered MIWI ubiquitination and removal by APC/C in late spermatogenesis. *Dev Cell*, **24**, 13-25.

34. Deng, W. and Lin, H. (2002) miwi, a murine homolog of piwi, encodes a cytoplasmic protein essential for spermatogenesis. *Dev Cell*, **2**, 819-830.

35. Zuo, H., Zhang, J., Zhang, L., Ren, X., Chen, X., Hao, H., Zhao, X. and Wang, D. (2016) Transcriptomic Variation during Spermiogenesis in Mouse Germ Cells. *PLoS One*, **11**, e0164874.

36. Gou, L.T., Dai, P., Yang, J.H., Xue, Y., Hu, Y.P., Zhou, Y., Kang, J.Y., Wang, X., Li, H., Hua, M.M. *et al*. (2014) Pachytene piRNAs instruct massive mRNA elimination during late spermiogenesis. *Cell Res*, **24**, 680-700.
37. Zhong, C., Yin, Q., Xie, Z., Bai, M., Dong, R., Tang, W., Xing, Y.H., Zhang, H., Yang, S., Chen, L.L. *et al*. (2015) CRISPR-Cas9-Mediated Genetic Screening in Mice with Haploid Embryonic Stem Cells Carrying a Guide RNA Library. *Cell Stem Cell*, **17**, 221-232.
38. Li, Z., Zhang, X., Xie, S., Liu, X., Fei, C., Huang, X., Tang, Y. and Zhou, L.Q. (2022) H3K36me2 methyltransferase NSD2 orchestrates epigenetic reprogramming during spermatogenesis. *Nucleic Acids Res*.
39. Bellve, A.R. (1993) Purification, culture, and fractionation of spermatogenic cells. *Methods Enzymol*, **225**, 84-113.
40. Kuramochi-Miyagawa, S., Watanabe, T., Gotoh, K., Totoki, Y., Toyoda, A., Ikawa, M., Asada, N., Kojima, K., Yamaguchi, Y., Ijiri, T.W. *et al*. (2008) DNA methylation of retrotransposon genes is regulated by Piwi family members MILI and MIWI2 in murine fetal testes. *Genes Dev*, **22**, 908-917.

Figure legends

Figure 1. Expression profiles of FBXO24 during testicular development and spermatogenesis in mice. (A) qPCR analysis of FBXO24 mRNA levels in multiple organs in mice. (B) qPCR analysis of FBXO24 mRNA levels in developing testes at postnatal day 0 (P0), P3, P7, P14, P28, and P35. (C) qPCR analysis of FBXO24 mRNA levels in isolated spermatogenic cell populations, including spermatogonia (SG), Sertoli cells (SE), spermatocytes (SC), round spermatids (RS), and elongating spermatids (ES). (D) Western blot analysis of FBXO24-HA expression in the tissues of adult transgenic mice. (E-F) Co-immunostaining of FBXO24-HA (red) and (E) γH2AX (green) or (F) PNA (green) in adult *Fbxo24*-HA testes. Scale bar, 25 μm. DNA (blue) is stained by DAPI. Spermatogenic stages are noted in (F).

Figure 2. FBXO24 deficiency male mice exhibits spermatogenic defects in the late steps of spermiogenesis. (A) qPCR analysis indicates that FBXO24 mRNA is markedly decreased in the testis of *Fbxo24* knockout (KO) as compared to wild-type (WT). ***, p< 0.001. (B) The fertility tests of WT and *Fbxo24* KO male mice mated with fertile female mice are shown. n = 3/group. Error bars represent mean ± S.D. ***, $p < 0.001$; ns: not significant. (C) Histological images of testes and epididymis of WT and *Fbxo24* KO mice at 8-weeks old are shown. (D) PAS-hematoxylin staining of *Fbxo24* KO testis at 8-weeks old contained less-condensed late spermatids (red arrows). Spermatogenic stages are noted. RS, round spermatids; ES, elongating spermatids; Pl, preleptotene; P, pachytene; Z, zygotene; D, diplotene. Scale bars = 25 μm. (E) The number of late spermatids is significantly reduced in *Fbxo24* KO testis. Ratios of spermatids and Sertoli cells in tubule cross-sections of specific stages of seminiferous epithelial cycles and corresponding spermatid development steps are shown. Data are mean ± S.D. *, p< 0.05. (F) Litter sizes of mating tests. F1 generation of intercrosses between the indicated males and *Fbxo24*+/− females are shown. Each dot represents one litter.

Figure 3. Sperm mitochondria and flagella were defective in FBXO24-deficient mice. (A-B) Quantification of sperm counts (A) and sperm motility (B) from WT and *Fbxo24* KO epididymis are shown. n = 3/group. Error bars represent mean ± S.D. **, $p < 0.01$. ***, $p < 0.001$. (C) Sperm morphological images show the defective sperm of *Fbxo24* KO mice. Red arrows indicate abnormal gaps in the mitochondrial sheath. Scale bars = 50 μm. (D) Immunofluorescence images of sperm from WT and *Fbxo24* KO epididymis. PNA (acrosome, green), MitoTracker (mitochondria, red), and DAPI (nucleus, blue). White arrows indicate the weak or absent staining of MitoTracker. (E) Quantifications of the length of sperm midpiece from WT and *Fbxo24* KO mice are shown. n = 100/group. Error bars represent mean ± S.D. ***, $p < 0.001$. (F) Scanning electronic microscopy (SEM) images indicate the mitochondria detachment from the flagellum of *Fbxo24* KO sperm. Right panel insets show higher magnification of sperm midpiece. The arrowheads indicate the annulus. The dashed red line indicates a region where mitochondria are absent. Scale bars = 2 μm. (G) Transmission electronic microscopy (TEM) images indicate the mitochondria defects in three regions of *Fbxo24* KO sperm midpiece in the longitudinal sections. Nu, Nucleus. The dashed red lines indicate a region where mitochondria are absent. The white arrowhead indicates sperm annulus. Scale bar = 0.2 μm. (H) TEM images indicate the ultrastructure of the midpiece, principal piece and end piece of WT and *Fbxo24* KO sperm flagellum in the cross-sections. Arrows indicate the mitochondria (MI), outer dense fiber (ODF) and axoneme. Scale bar = 0.2 μm. (I-J) Western blot shows the levels of proteins of mitochondria (I) and axoneme (J) of WT and *Fbxo24* KO sperm.

GAPDH serves as a loading control.

Figure 4. Ablation of FBXO24 affects mitochondria and chromatoid body architecture in the round spermatids. (A) TEM images show swollen mitochondria with disorganized cristae in the round spermatids of *Fbxo24* KO testes. Right panel insets show higher magnification of mitochondria. Scale bars = 1 μm. (B) Quantification of the number of swollen mitochondria in (C). ***, $p < 0.001$. (C) TEM images showing decondensed and enlarged chromatoid body (CB) with an irregular network in the round spermatids of *Fbxo24* KO testes. Right panel insets show a higher magnification of CB. Scale bars = 1 μm. (D) Quantification of size/diameters of CB in (A). *, $p < 0.05$. (E) Western blot analysis expression levels of CB components and PRMT6 in testes from WT and *Fbxo24* KO mice at 8 weeks old. GAPDH serves as a loading control.

Figure 5. FBXO24 deficiency in mice impairs sperm histone-to-protamine exchange. (A) SEM images show the abnormality of *Fbxo24* KO sperm head. AA, anterior acrosome; EQ, equatorial segment; PAS, postacrosomal segment; VS, ventral spur; HR, hook rim. Scale bars = 2 μm. (B) TEM images show the decondensed nucleus (Nu) of *Fbxo24* KO sperm. Scale bars = 1 μm. (C) Western blot analysis of the expression of histones (H2A, H2B, H3, and H4), transition proteins (TNP1), and protamines (PRM2) from WT and *Fbxo24* KO sperm are shown. GAPDH serves as a loading control. (D) Quantification of protein levels in (C). Error bars represent mean ± S.D., n = 3. *, $p < 0.05$. (E) Western blot analysis of the expression of indicated proteins in WT and *Fbxo24* KO testis. GAPDH serves as a loading control. (F) Quantification of protein levels in (E). Error bars represent mean ± S.D., n = 3. *, $p < 0.05$.

Figure 6. RNA-seq analyses of the round spermatids from FBXO24-deficient testes. (A) Volcano plot of differentially expressed transcripts in the round spermatids (RS) of *Fbxo24* KO *vs*. WT mice. Each red (up-regulation) or blue (down-regulation) dot represents a significantly changed gene. (B) GO term enrichment analysis of downregulated transcripts of *Fbxo24* KO RS. (C-D) Gene expressions of mitochondrion localization (C) and chromatin organization (D) in RNA-seq analysis. (E) Venn diagrams showing the overlap between downregulated genes and abnormal alternative splicing genes in *Fbxo24* KO RS. (F) Summary of differential splicing evens in *Fbxo24* KO RS. The number of each category of alternative splicing is indicated.

Figure 7. Aberrant alternative splicing of spermiogenesis genes in the round spermatids of FBXO24-deficient mice. (A) Co-immunoprecipitation analysis of FBXO24 and the splicing regulators (SRSF2, SRSF3, and SRSF9) in *Fbxo24*-HA tagged mice testis. WT testis was used as a negative control. (B) Western blotting analysis of the splicing regulators in WT and *Fbxo24* KO testis. GAPDH was used as a loading control. (C) Quantification of protein levels in (B). Error bars represent mean ± S.D., n = 3. *, $p < 0.05$. (D-H) Validation of abnormal alternative splicing genes related to (D) mitochondria (*Mfn1*), (E) flagellum (*Zmynd12*, *Map7d1*, and *Bbs7*), (F) chromatin (*Phf7* and *Kat5*), (G) acrosome (*Nucb2*), and (H) ubiquitination (*Ube2j2*). The top panels represent RT-PCR analysis of indicated genes in WT and *Fbxo24* RS. The middle panels show the quantification of percent spliced in (PSI) and alternative sites in RNA-seq. Error bars represent mean ± S.D., n = 2. *, $p < 0.05$. The bottom panels represent the schematic diagram of alternative sites exons.

Figure 8. FBXO24 interacts with MIWI and mediates its K48-linked polyubiquitination. (A) HEK293T cells transfected with empty FBXO24-mCherry or mCherry vector. Anti-mCherry beads were used for immunoprecipitation (IP), and western blots were adopted to detect the CUL1 (left panel) and MIWI (right panel) expression. (B) The testis lysate of *Fbxo24*-HA tagged mice were immunoprecipitated with anti-HA beads. Western blots were adopted to detect the HA, CUL1, MIWI, SKP1, and RBX1expression. (C) Schematic structures of the truncated FBXO24 protein are shown. Broken boxes show the F-box and regulator of chromosome condensation 1 (RCC1) domains. (D) HEK293T cells were transfected with indicated plasmids. Immunoprecipitation was performed using the anti-mCherry antibody. (E) Western blot analysis of HEK293T cells transfected with indicated FBXO24-mCherry and 2μg MIWI-myc plasmids. The cell lysates were immunoblotted with anti-mCherry and anti-Myc antibodies. (F) FBXO24 mediated the ubiquitination of MIWI in the presence of Ub(K48) not Ub (K63). (G) HEK293T cells were transfected with indicated FBXO24-mCherry, 2μg MIWI-myc, and 2μg Ub-HA plasmids. The cell lysates were immunoblotted with the anti-mCherry, anti-Myc, and anti-HA antibodies. GAPDH serves as a loading control. The cells were treated with MG132 (10 μM) in the ubiquitination assay.

Figure 9. Small RNA-seq analysis of testes from FBXO24-deficient mice. (A) A scatter plot of differentially expressed miRNA is shown. Red and green dots represent up- and down-regulated miRNA (fold change > 2, $p<0.05$), respectively. (B) Genomic distribution of piRNA profile in *Fbxo24* KO *vs*. WT tesis. piRNA levels were examined in each 200 bp interval of a 2 kb region upstream and downstream of the annotated genes. (C) Scatter plots of differentially expressed piRNA mapping density (reads/kb) of the coding region (CDS), 5′ and 3′ untranslated region (UTR), and intron, as well as transposable element (TE), including retrotransposon (LTR, LINE, and SINE) and DNA transposon. The piRNA read counts were normalized with miRNA. Red and green dots represent up- and down-regulated piRNA (fold change > 2, $p<0.05$), respectively. (D) The size distribution of piRNAs in *Fbxo24* KO *vs*. WT testis. (E) The top 10 up-regulated piRNAs in *Fbxo24* KO testis exist in MIWI immunoprecipitates of GSM822760 data.

Figure 10. A schematic model shows the FBXO24-mediated post-transcriptional regulation during spermiogenesis. Fbxo24 binds key splicing factors (SRSF2, SRSF3, and SRSF9) to coordinate proper alternative splicing of the target mRNA transcripts involved in spermiogenesis.

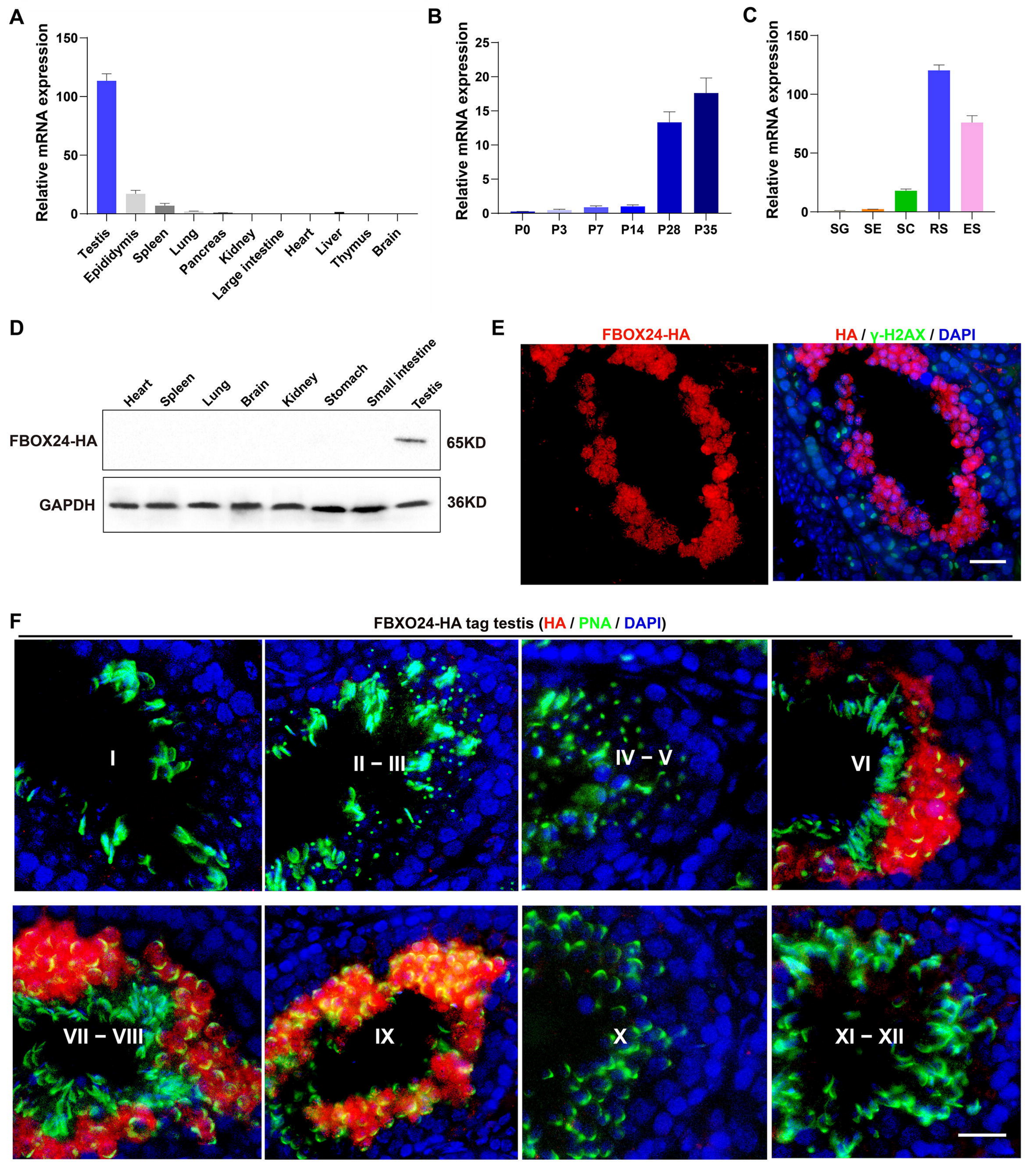
A
Relative mRNA expression
150
100
50
0
Testis
Epididymis
Spleen
Lung
Pancreas
Kidney
Large intestine
Heart
Liver
Thymus
Brain
B
Relative mRNA expression
25
20
15
10
5
0
P0
P3
P7
P14
P28
P35
C
Relative mRNA expression
150
100
50
0
SG
SE
SC
RS
ES
D
Heart
Spleen
Lung
Brain
Kidney
Stomach
Small intestine
Testis
FBOX24-HA
65KD
GAPDH
36KD
E
FBOX24-HA
HA / γ-H2AX / DAPI
F
FBXO24-HA tag testis (HA / PNA / DAPI)
I
II – III
IV – V
VI
VII – VIII
IX
X
XI – XII

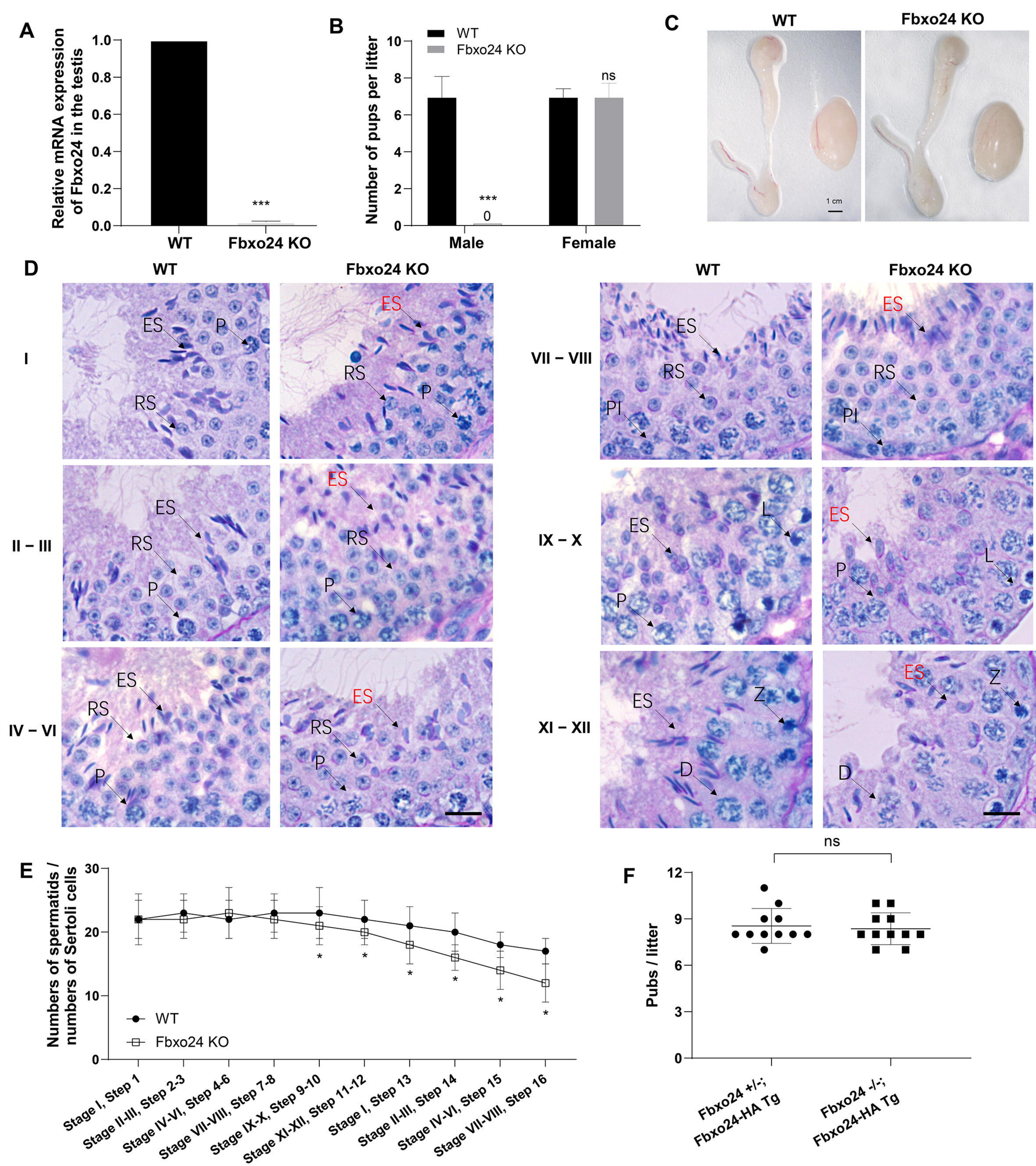
A
Relative mRNA expression of Fbxo24 in the testis
1.0
0.8
0.6
0.4
0.2
0.0
***
WT
Fbxo24 KO
B
Number of pups per litter
WT
Fbxo24 KO
10
8
6
4
2
0
***
0
ns
Male
Female
C
WT
Fbxo24 KO
1 cm
D
WT
Fbxo24 KO
I
II – III
IV – VI
VII – VIII
IX – X
XI – XII
ES
P
RS
PI
L
Z
D
E
Numbers of spermatids / numbers of Sertoli cells
30
20
10
0
WT
Fbxo24 KO
Stage I, Step 1
Stage II-III, Step 2-3
Stage IV-VI, Step 4-6
Stage VII-VIII, Step 7-8
Stage IX-X, Step 9-10
Stage XI-XII, Step 11-12
Stage I, Step 13
Stage II-III, Step 14
Stage IV-VI, Step 15
Stage VII-VIII, Step 16
F
ns
Pubs / litter
12
9
6
3
0
Fbxo24 +/-; Fbxo24-HA Tg
Fbxo24 -/-; Fbxo24-HA Tg

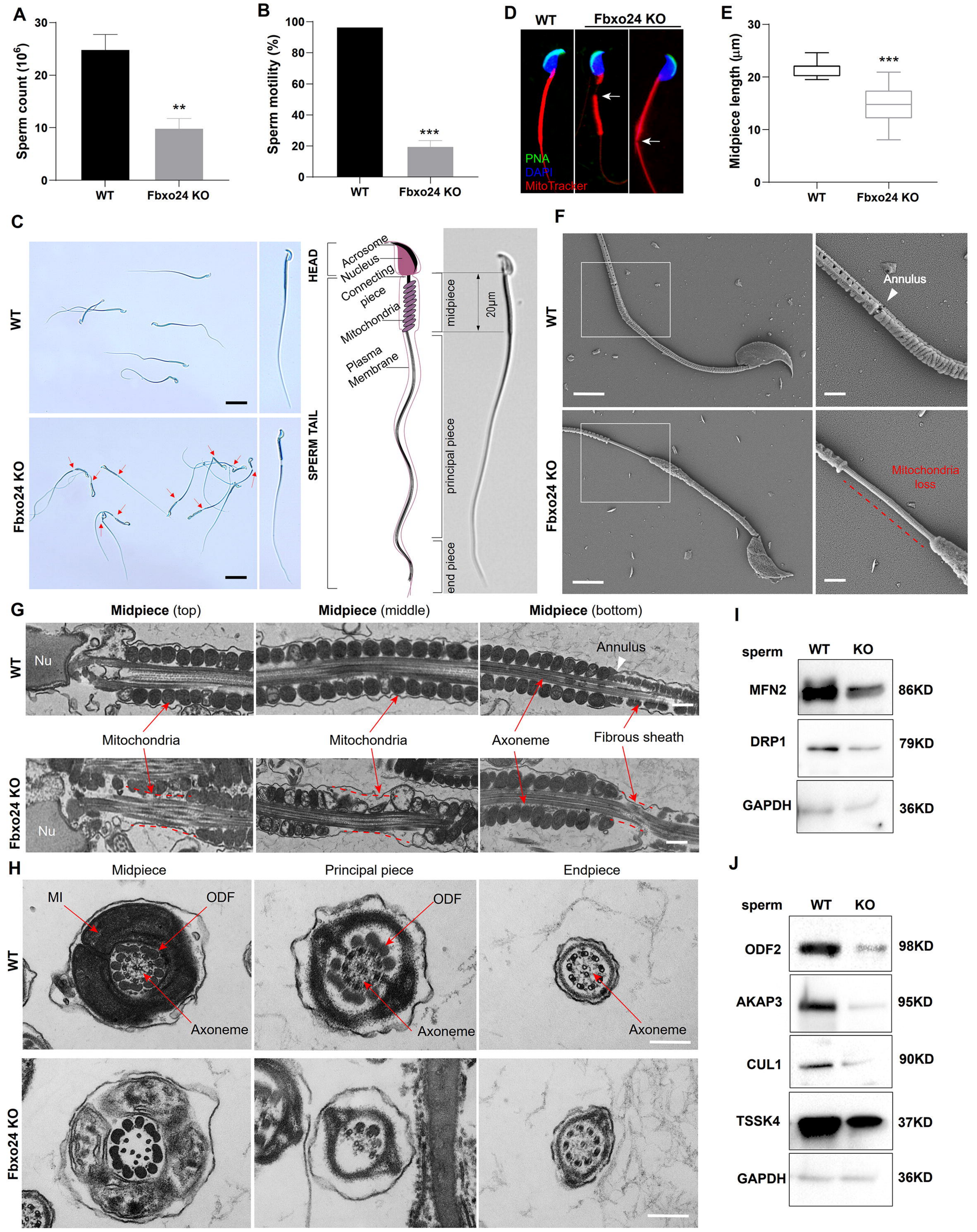
A
Sperm count (10^6)
30
20
10
0
**
WT
Fbxo24 KO
B
Sperm motility (%)
100
80
60
40
20
0
***
WT
Fbxo24 KO
D
WT
Fbxo24 KO
PNA
DAPI
MitoTracker
E
Midpiece length (μm)
30
20
10
0
***
WT
Fbxo24 KO
C
WT
Fbxo24 KO
HEAD
SPERM TAIL
Acrosome
Nucleus
Connecting piece
Mitochondria
Plasma Membrane
midpiece
20μm
principal piece
end piece
F
WT
Fbxo24 KO
Annulus
Mitochondria loss
G
Midpiece (top)
Midpiece (middle)
Midpiece (bottom)
WT
Fbxo24 KO
Nu
Annulus
Mitochondria
Mitochondria
Axoneme
Fibrous sheath
H
Midpiece
Principal piece
Endpiece
WT
Fbxo24 KO
MI
ODF
ODF
Axoneme
Axoneme
Axoneme
I
sperm
WT
KO
MFN2
86KD
DRP1
79KD
GAPDH
36KD
J
sperm
WT
KO
ODF2
98KD
AKAP3
95KD
CUL1
90KD
TSSK4
37KD
GAPDH
36KD

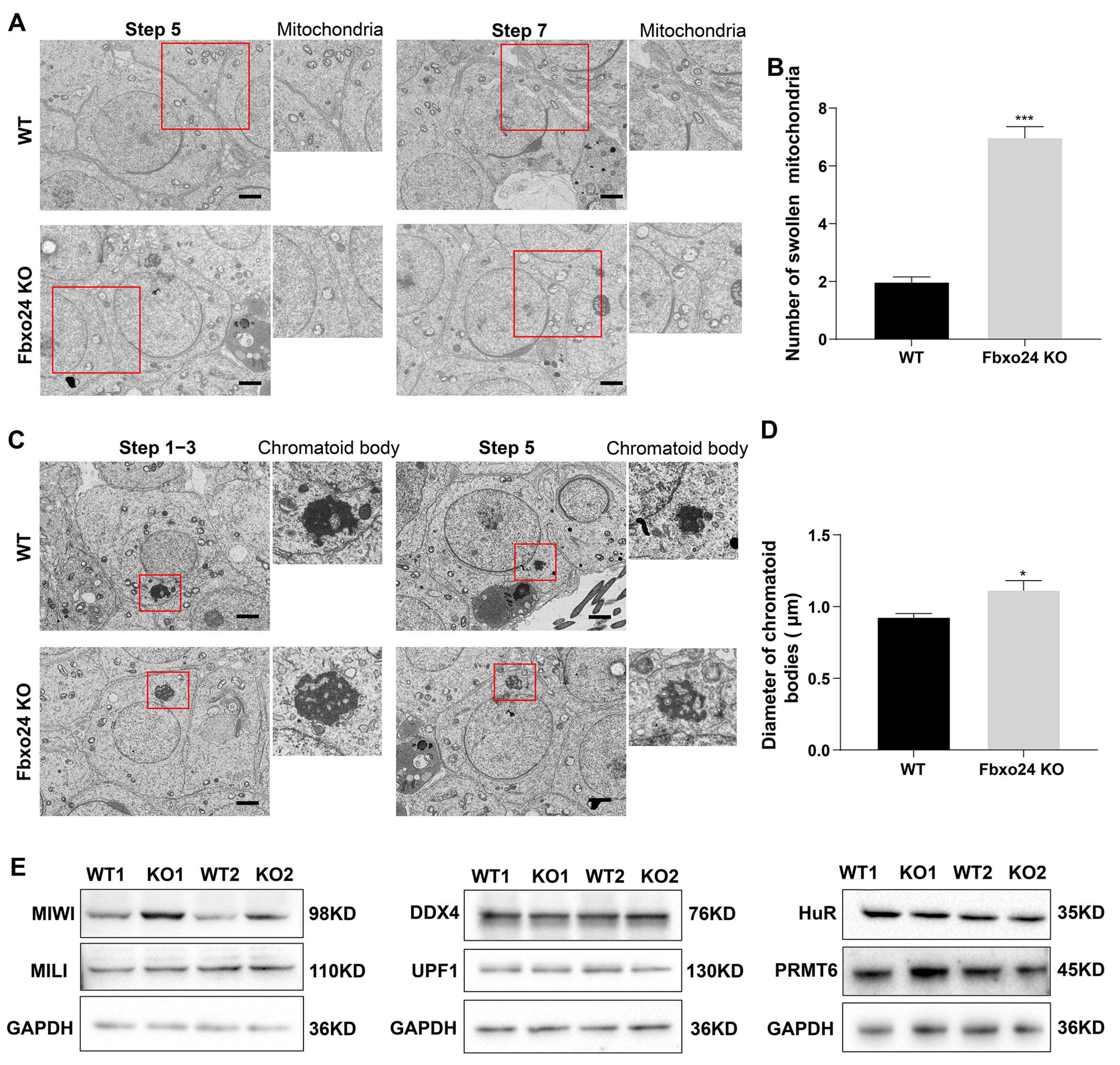
A
Step 5
Mitochondria
Step 7
Mitochondria
WT
Fbxo24 KO
B
Number of swollen mitochondria
8
6
4
2
0
***
WT
Fbxo24 KO
C
Step 1−3
Chromatoid body
Step 5
Chromatoid body
WT
Fbxo24 KO
D
Diameter of chromatoid bodies (μm)
1.5
1.0
0.5
0.0
*
WT
Fbxo24 KO
E
WT1 KO1 WT2 KO2
MIWI
98KD
MILI
110KD
GAPDH
36KD
WT1 KO1 WT2 KO2
DDX4
76KD
UPF1
130KD
GAPDH
36KD
WT1 KO1 WT2 KO2
HuR
35KD
PRMT6
45KD
GAPDH
36KD

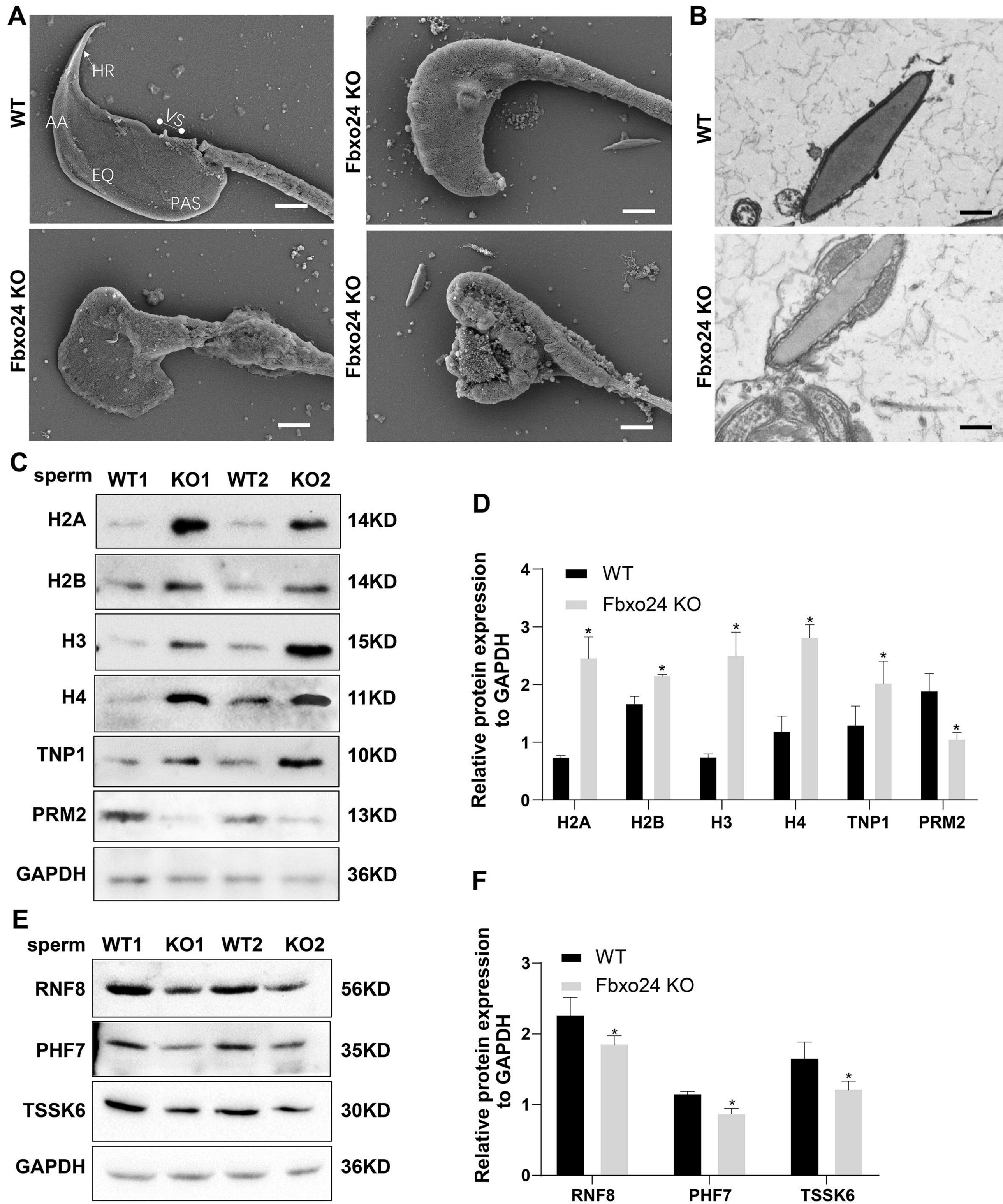
A
WT
HR
AA
VS
EQ
PAS
Fbxo24 KO
Fbxo24 KO
Fbxo24 KO
B
WT
Fbxo24 KO
C
sperm
WT1
KO1
WT2
KO2
H2A
14KD
H2B
14KD
H3
15KD
H4
11KD
TNP1
10KD
PRM2
13KD
GAPDH
36KD
D
Relative protein expression to GAPDH
WT
Fbxo24 KO
H2A
H2B
H3
H4
TNP1
PRM2
E
sperm
WT1
KO1
WT2
KO2
RNF8
56KD
PHF7
35KD
TSSK6
30KD
GAPDH
36KD
F
Relative protein expression to GAPDH
WT
Fbxo24 KO
RNF8
PHF7
TSSK6

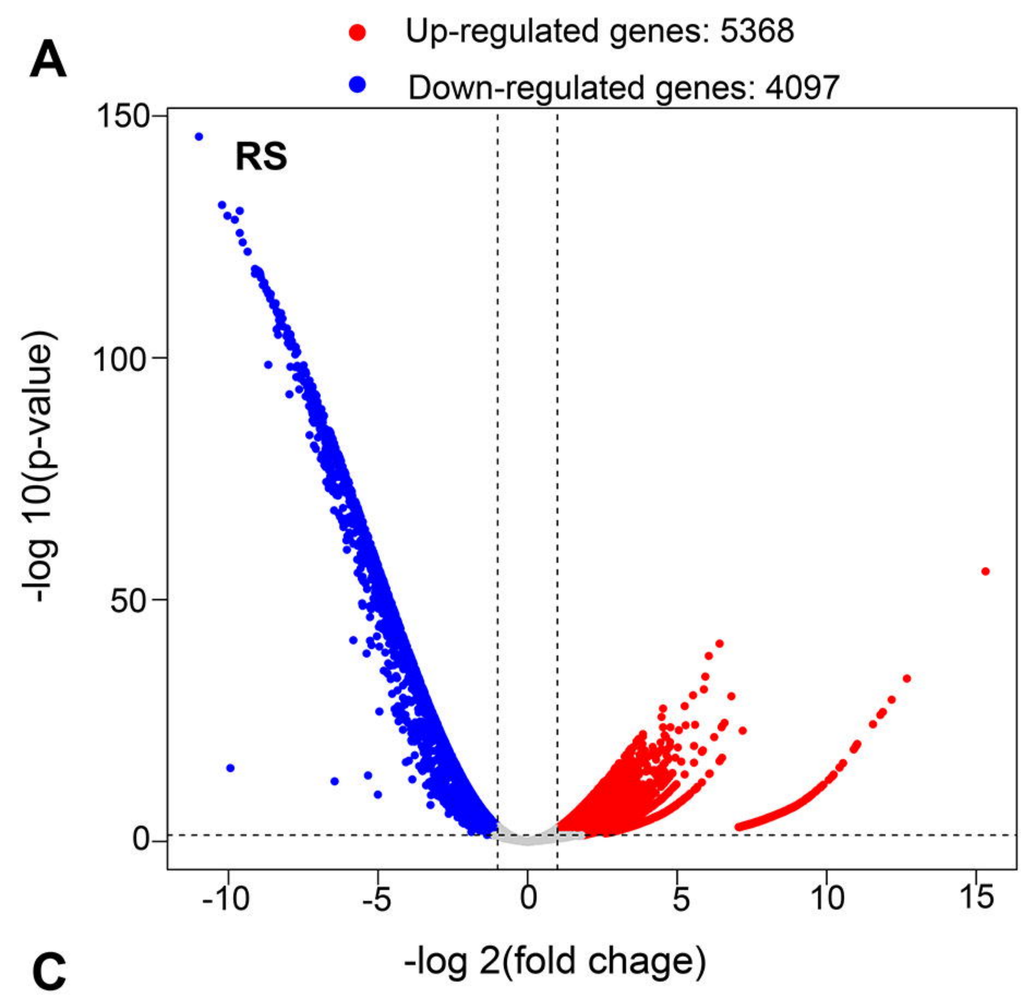
A
Up-regulated genes: 5368
Down-regulated genes: 4097
RS
-log 10(p-value)
-log 2(fold chage)

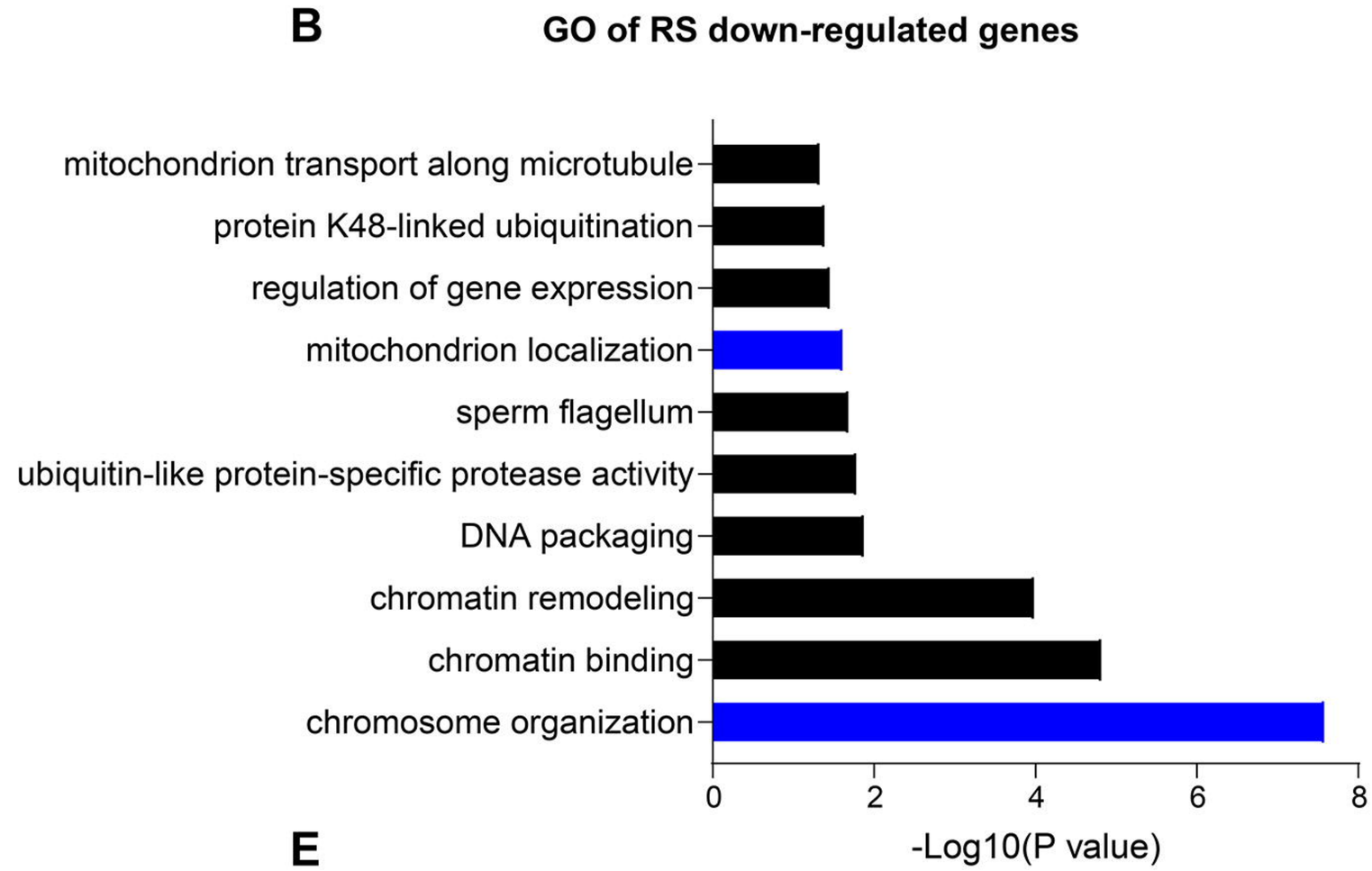
B
GO of RS down-regulated genes
mitochondrion transport along microtubule
protein K48-linked ubiquitination
regulation of gene expression
mitochondrion localization
sperm flagellum
ubiquitin-like protein-specific protease activity
DNA packaging
chromatin remodeling
chromatin binding
chromosome organization
-Log10(P value)

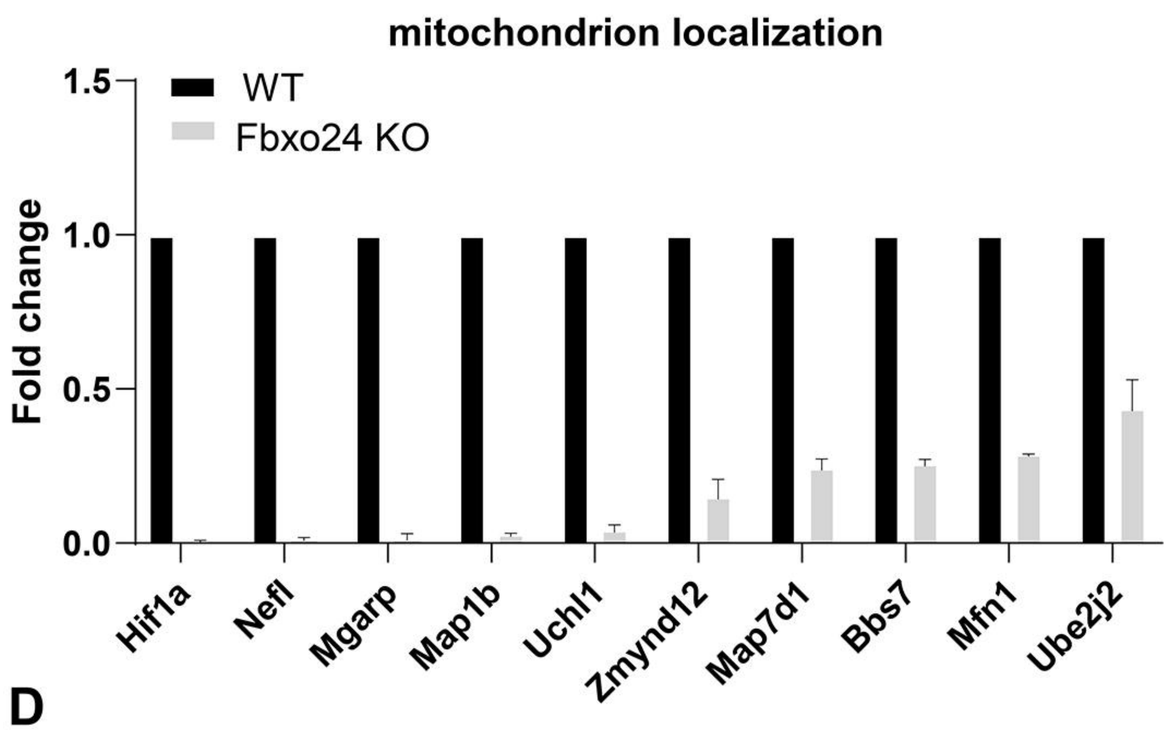
C
mitochondrion localization
WT
Fbxo24 KO
Fold change
Hif1a
Nefl
Mgarp
Map1b
Uchl1
Zmynd12
Map7d1
Bbs7
Mfn1
Ube2j2

E
RS down expressed genes
RS alternative spliced genes
3759
338
655

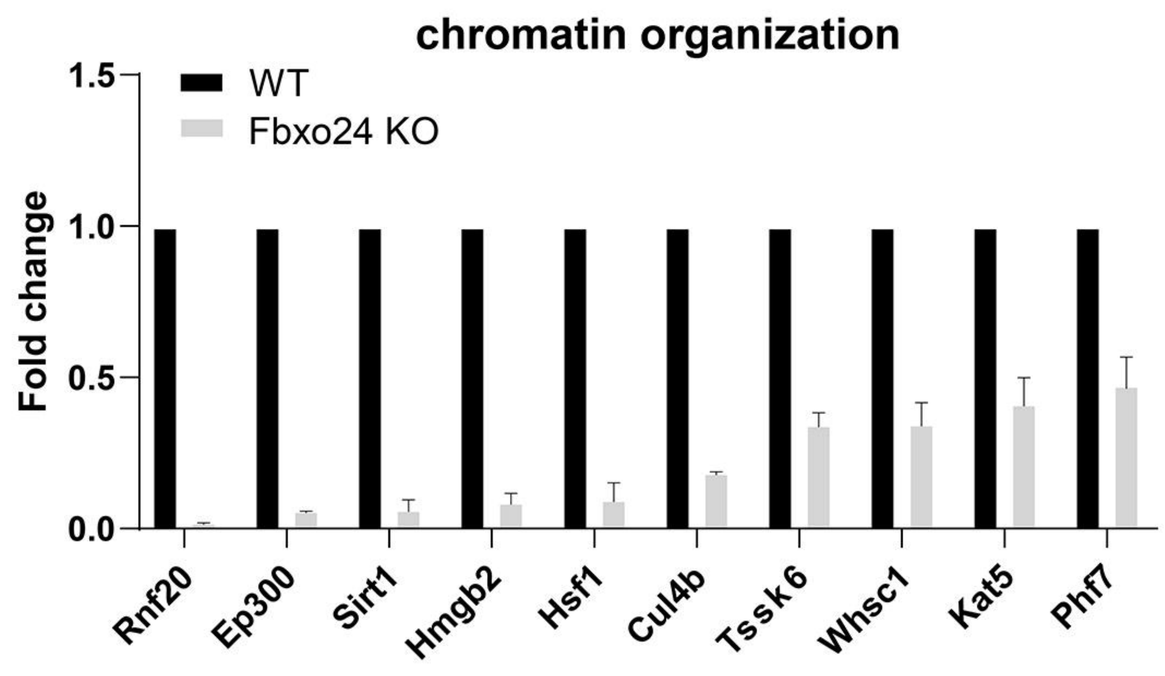
D
chromatin organization
WT
Fbxo24 KO
Fold change
Rnf20
Ep300
Sirt1
Hmgb2
Hsf1
Cul4b
Tssk6
Whsc1
Kat5
Phf7

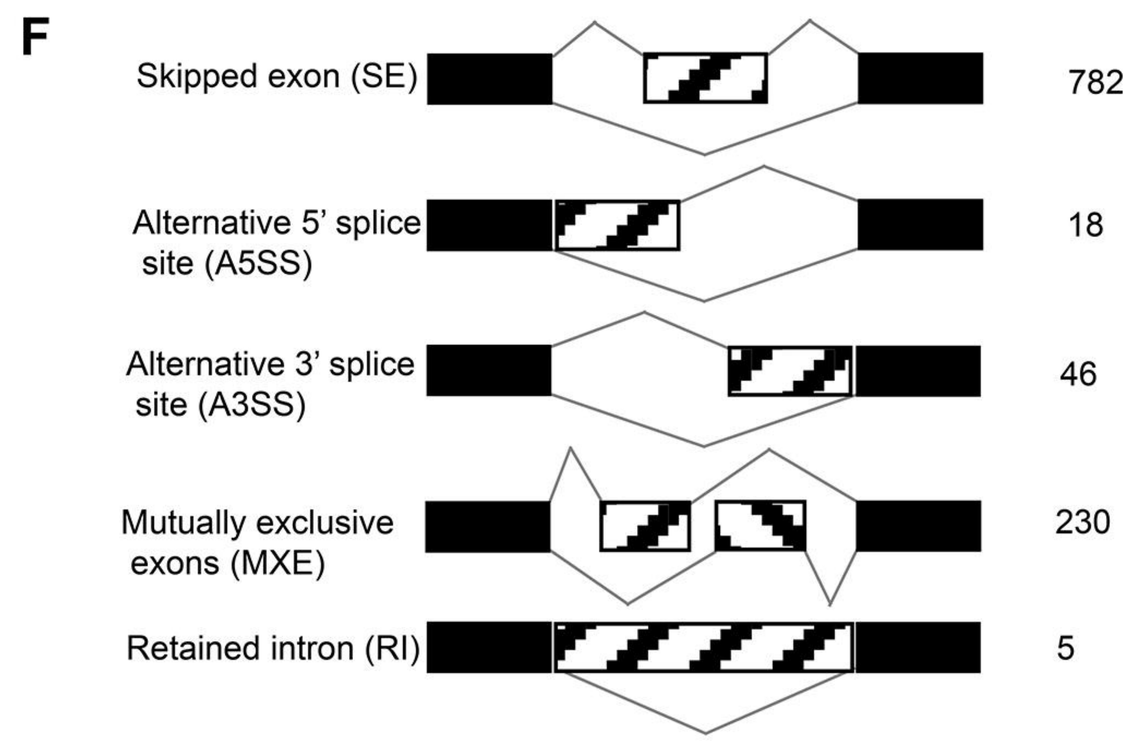
F
Skipped exon (SE)
782
Alternative 5' splice site (A5SS)
18
Alternative 3' splice site (A3SS)
46
Mutually exclusive exons (MXE)
230
Retained intron (RI)
5

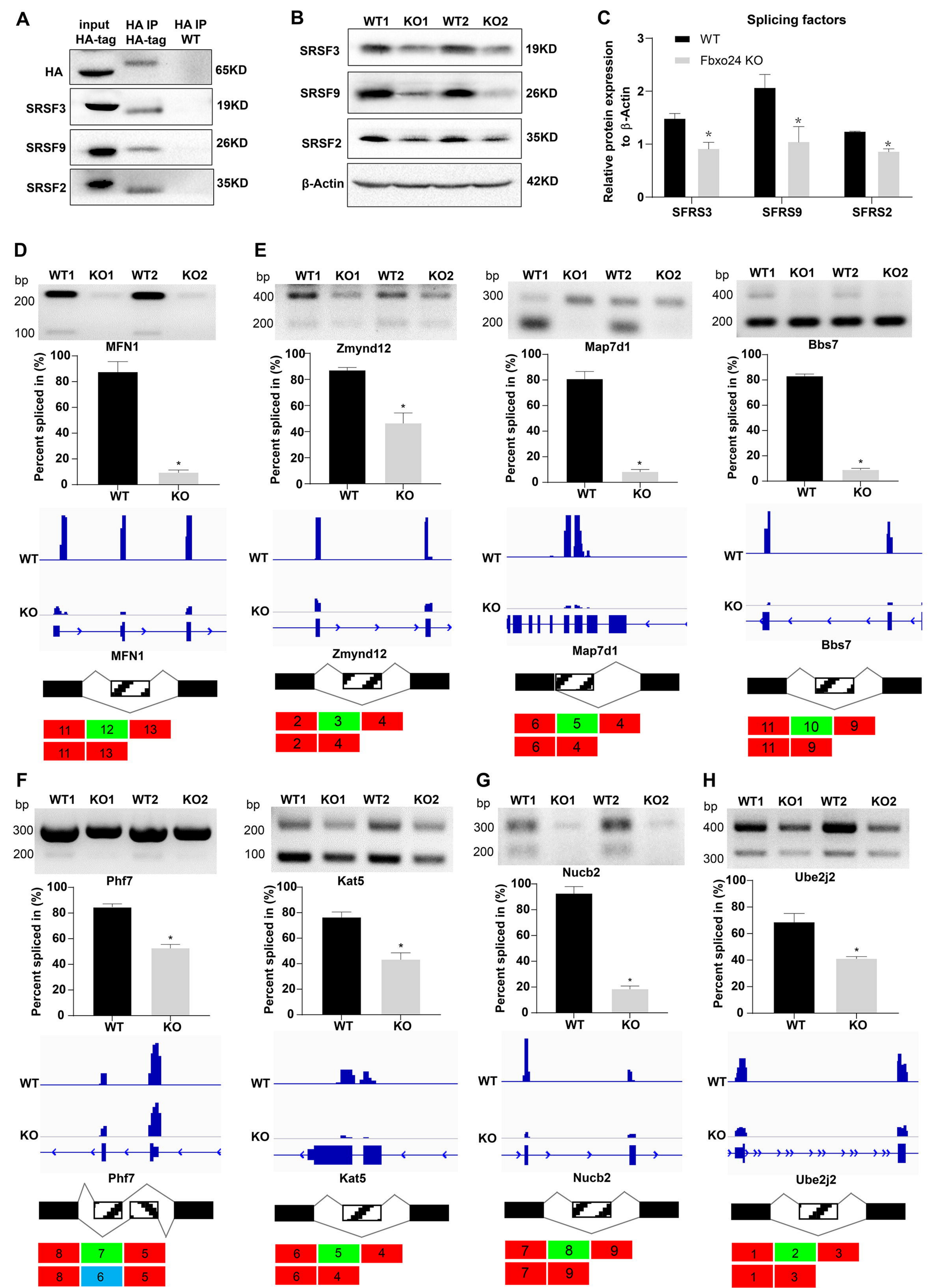
A
input HA-tag
HA IP HA-tag
HA IP WT
HA
SRSF3
SRSF9
SRSF2
65KD
19KD
26KD
35KD
B
WT1 KO1 WT2 KO2
SRSF3
SRSF9
SRSF2
β-Actin
19KD
26KD
35KD
42KD
C
Splicing factors
WT
Fbxo24 KO
Relative protein expression to β-Actin
SFRS3
SFRS9
SFRS2
D
bp
WT1 KO1 WT2 KO2
200
100
MFN1
Percent spliced in (%)
WT
KO
E
bp
WT1 KO1 WT2 KO2
400
200
Zmynd12
300
Map7d1
Bbs7
F
300
200
Phf7
100
Kat5
G
Nucb2
H
400
Ube2j2

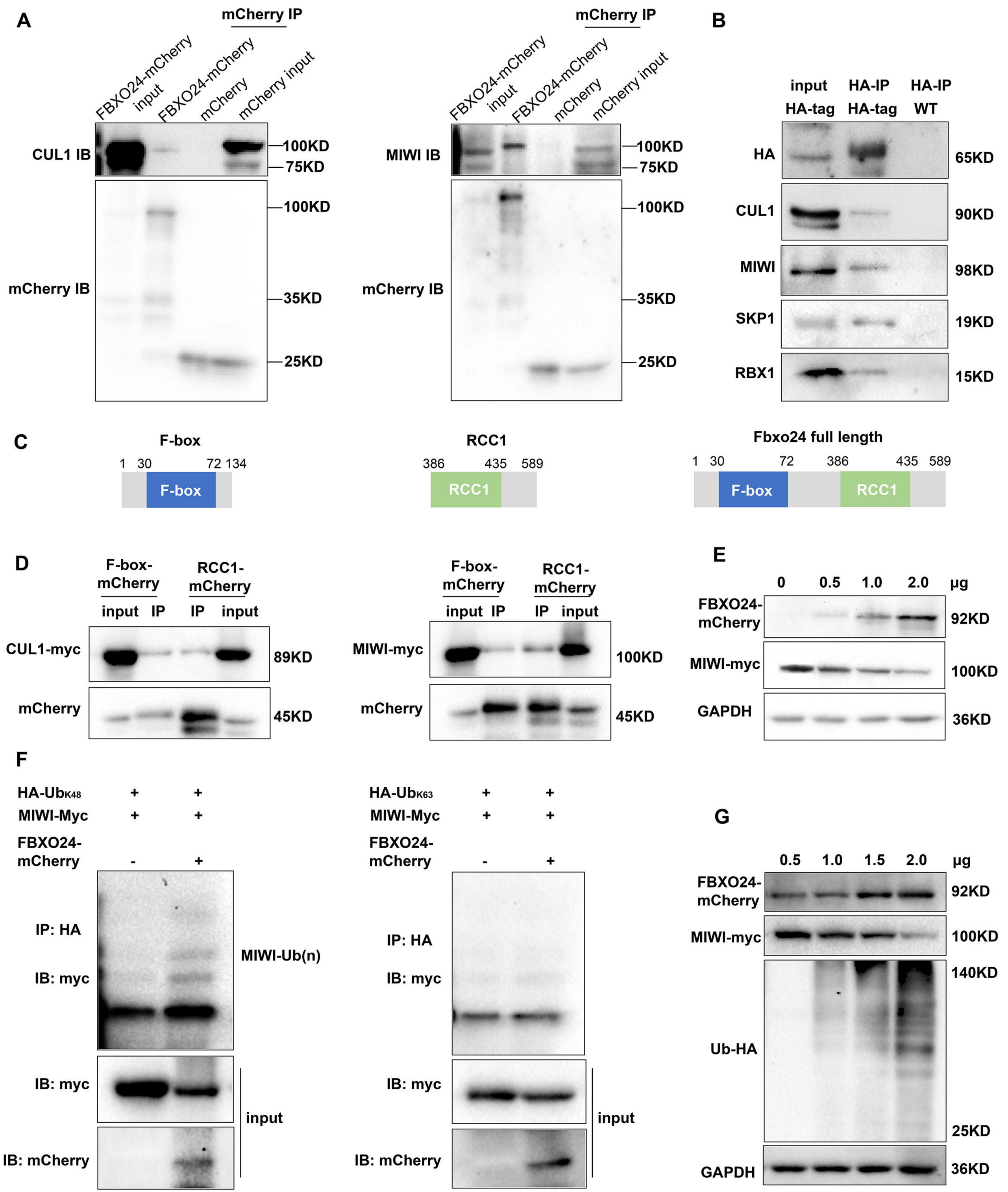
A
mCherry IP
FBXO24-mCherry input
FBXO24-mCherry
mCherry
mCherry input
CUL1 IB
100KD
75KD
mCherry IB
100KD
35KD
25KD
MIWI IB
B
input HA-tag
HA-IP HA-tag
HA-IP WT
HA
65KD
CUL1
90KD
MIWI
98KD
SKP1
19KD
RBX1
15KD
C
F-box
1 30 72 134
RCC1
386 435 589
Fbxo24 full length
1 30 72 386 435 589
D
F-box-mCherry
RCC1-mCherry
input IP IP input
CUL1-myc
89KD
mCherry
45KD
MIWI-myc
100KD
E
0 0.5 1.0 2.0 μg
FBXO24-mCherry
92KD
MIWI-myc
100KD
GAPDH
36KD
F
HA-UbK48
HA-UbK63
MIWI-Myc
FBXO24-mCherry
IP: HA
IB: myc
MIWI-Ub(n)
IB: mCherry
input
G
0.5 1.0 1.5 2.0 μg
140KD
Ub-HA
25KD

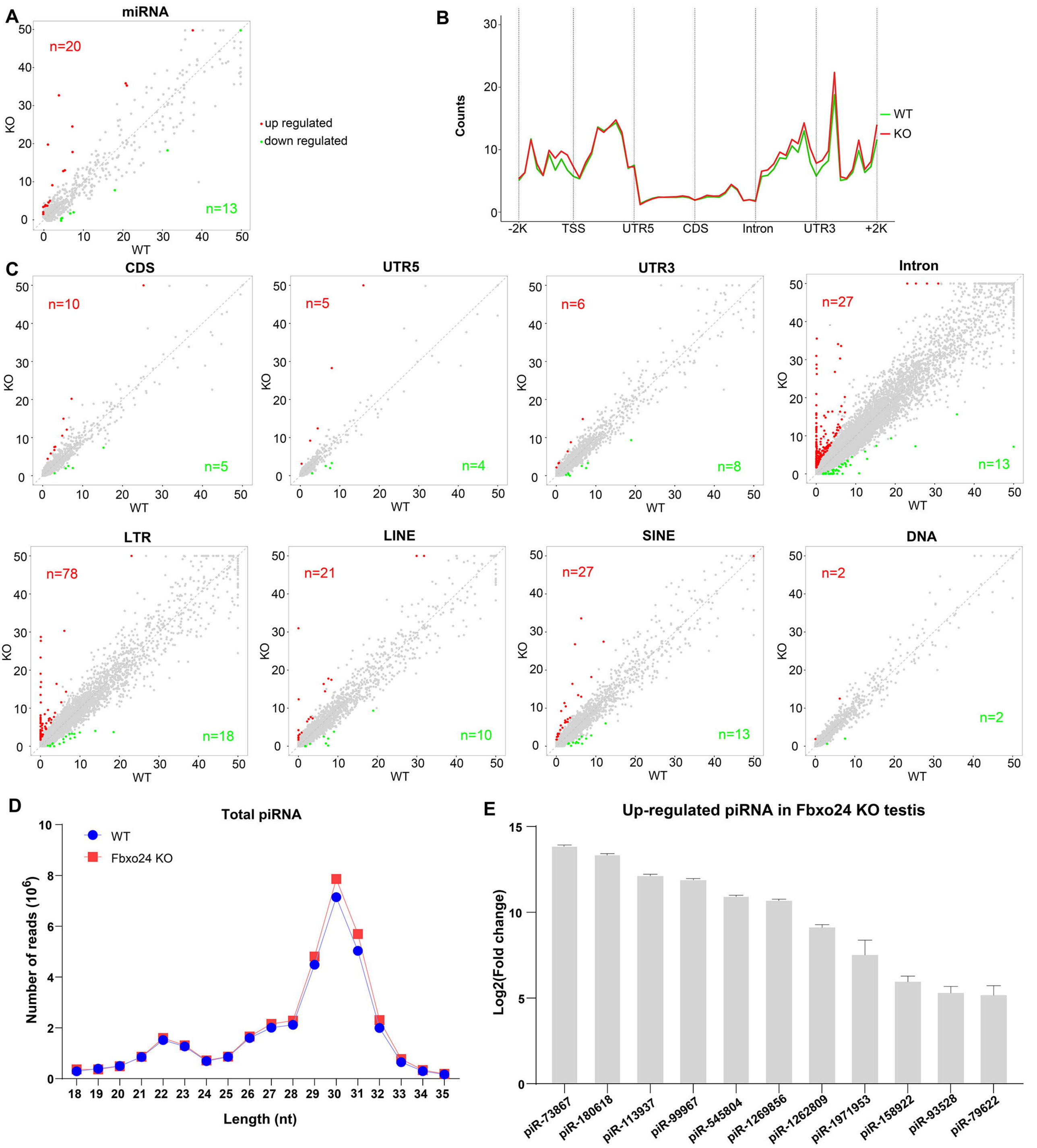
A
miRNA
n=20
n=13
up regulated
down regulated
KO
WT
B
Counts
WT
KO
-2K
TSS
UTR5
CDS
Intron
UTR3
+2K
C
CDS
n=10
n=5
UTR5
n=5
n=4
UTR3
n=6
n=8
Intron
n=27
n=13
LTR
n=78
n=18
LINE
n=21
n=10
SINE
n=27
n=13
DNA
n=2
n=2
D
Total piRNA
WT
Fbxo24 KO
Number of reads (10^6)
Length (nt)
E
Up-regulated piRNA in Fbxo24 KO testis
Log2(Fold change)
piR-73867
piR-180618
piR-113937
piR-99967
piR-545804
piR-1269856
piR-1262809
piR-1971953
piR-158922
piR-93528
piR-79622

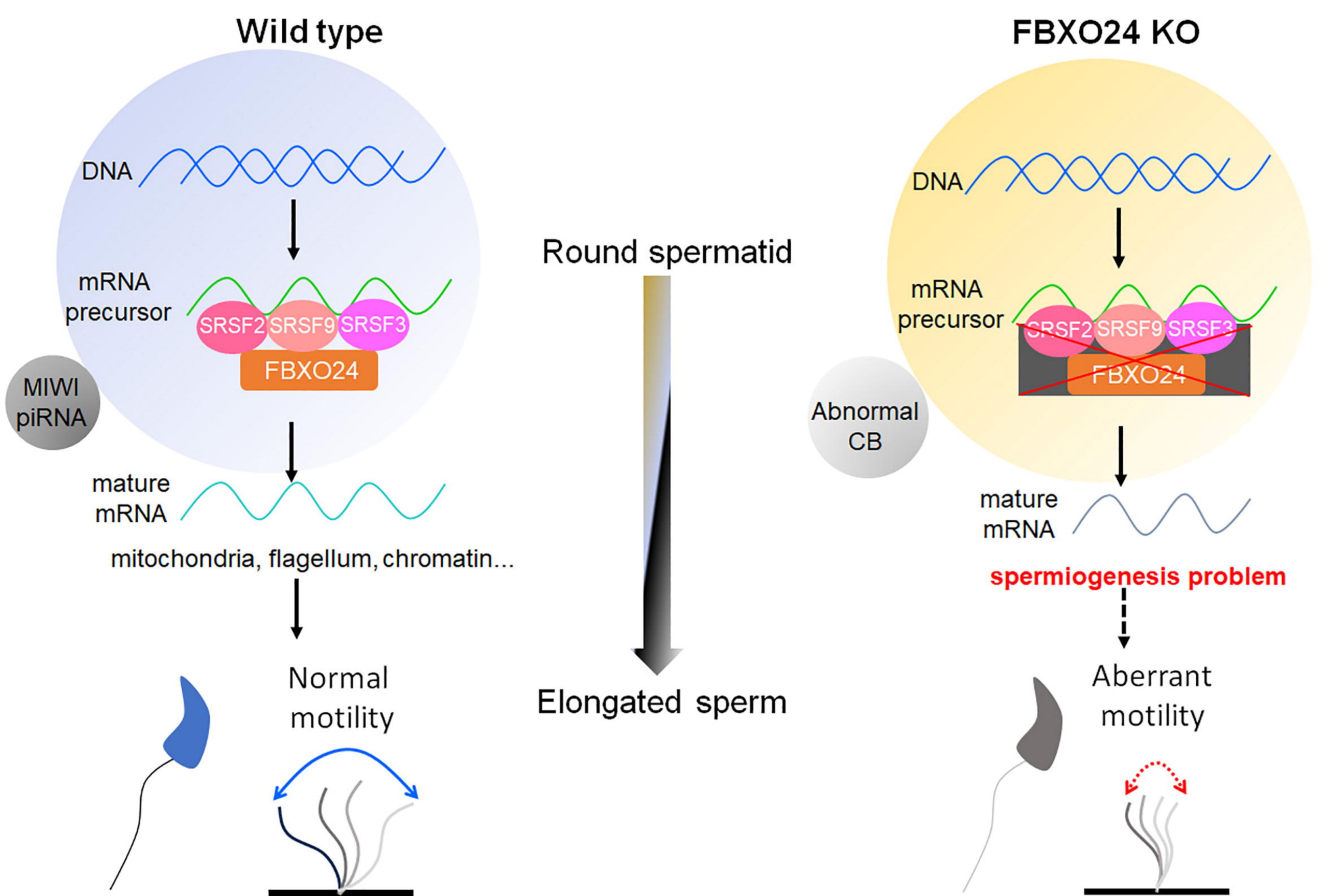
Wild type
FBXO24 KO
DNA
mRNA
precursor
SRSF2
SRSF9
SRSF3
FBXO24
MIWI
piRNA
mature
mRNA
mitochondria, flagellum, chromatin...
Normal
motility
Round spermatid
Elongated sperm
DNA
mRNA
precursor
SRSF2
SRSF9
SRSF3
FBXO24
Abnormal
CB
mature
mRNA
spermiogenesis problem
Aberrant
motility